Real-Time Adaptive Drag Minimization Wind Tunnel Investigation of a Flexible Wing with Variable Camber Continuous Trailing Edge Flap System

Nhan Nguyen*
Nicholas Cramer†
Kelley Hashemi‡
NASA Ames Research Center, Moffett Field, CA 94035
Michael Drew§
Stinger Ghaffarian Technologies, Inc., Moffett Field, CA 94035
Richard Wise¶
Jovan Boskovic‖
Scientific Systems Company, Inc., Woburn, MA 01801
Nathan Precup**
Tyler Mundt††
Eli Livne‡‡
University of Washington, Seattle, WA 98195

This paper reports the results of a recently completed real-time adaptive drag minimization wind tunnel investigation of a highly flexible wing wind tunnel model equipped with the Variable Camber Continuous Trailing Flap (VCCTEF) technology at the University of Washington Aeronautical Laboratory (UWAL). The wind tunnel investigation is funded by NASA SBIR Phase II contract with Scientific Systems Company, Inc. (SSCI) and University of Washington (UW) as a subcontractor. The wind tunnel model is a sub-scale Common Research Model (CRM) wing constructed of foam core and fiberglass skin and is aeroelastically scaled to achieve a wing tip deflection of 10% of the wing semi-span which represents a typical wing tip deflection for a modern transport such as Boeing 787. The jig-shape twist of the CRM wing is optimized using a CART3D aero-structural model to achieve the minimum induced drag for the design cruise lift coefficient of 0.5. The wing is equipped with two chordwise cambered segments for each of the six spanwise flap sections for a total of 12 individual flap segments that comprise the VCCTEF system. Each of the 12 flap segments is actively controlled by an electric servo-actuator.

The real-time adaptive drag optimization strategy includes an on-board aerodynamic model identification, a model excitation, and a real-time drag optimization. The on-board aerodynamic model is constructed parametrically as a function of the angle of attack and flap positions to model the lift and drag coefficients of the wing. The lift coefficient models include a linear model and a second-order model. The drag coefficient models include a quadratic model and a higher-order up to 6^{th}-order model to accurately model the drag coefficient at high angles of attack. The onboard aerodynamic model identification includes a recursive least-squares

*Senior Research Scientist and Technical Group Lead, Intelligent Systems Division, nhan.t.nguyen@nasa.gov
†Aerospace Engineer, Intelligent Systems Division, nicholas.b.cramer@nasa.gov
‡Aerospace Engineer, Intelligent Systems Division, kelley.e.hashemi@nasa.gov
§Aerospace Engineer, Intelligent Systems Division, michael.c.drew@nasa.gov
¶Lead Applications Engineer, Intelligent & Autonomous Control Systems, Richard.Wise@ssci.com
‖Principal Research Engineer and Senior Group Leader, Intelligent & Autonomous Control Systems, Jovan.Boskovic@ssci.com
**Graduate students, William E. Boeing Department of Aeronautics and Astronautics, eli@aa.washington.edu
††Graduate students, William E. Boeing Department of Aeronautics and Astronautics, eli@aa.washington.edu
‡‡Boeing Endowed Professor of Aeronautics and Astronautics, William E. Boeing Department of Aeronautics and Astronautics, eli@aa.washington.edu

(RLS) algorithm and a batch least-squares (BLS) algorithm designed to estimate the model parameters. The model excitation method is designed to sample the input set that comprises the angle of attack and the flap positions. Three model excitation methods are developed: random excitation method, sweep method, and iterative angle-of-attack seeking method. The real-time drag optimization includes a generic algorithm developed by SSCI and several optimization methods developed by NASA which include a second-order gradient Newton-Raphson optimization method, an iterative gradient optimization method, a pseudo-inverse optimization method, an analytical optimization method, and an iterative refinement optimization method.

The first wind tunnel test entry took place in September 2017. This test revealed major hardware issues and required further redesign of the flap servo mechanisms.

The second test entry took place in April 2018. However, the test was not successful due to the issues with the onboard aerodynamic model identification RLS algorithm which incorrectly identified model parameters. This test also provides an experimental comparison study between the VCCTEF and a variable camber discrete trailing edge flap (VCDTEF) without the elastomer transition mechanisms. The experimental result confirms the benefit of the VCCTEF which produces lower drag by 5% than the VCDTEF.

The third and final test entry took place in June 2018 after the issues with the RLS algorithm have been identified and corrected. Additional improvements were implemented. These include the BLS algorithm, the iterative angle-of-attack seeking method, the iterative gradient optimization method, and the pseudo-inverse optimization method. The test objectives were successfully demonstrated as the real-time drag optimization identifies several optimal solutions at off-design lift coefficients. The iterative gradient optimization method is found to achieve up to 4.7% drag reduction for the off-design lift coefficient of 0.7. The pseudo-inverse optimization method which does not require the drag coefficient model is found to be quite effective in reducing drag. Up to 9.4% drag reduction for the off-design lift coefficient of 0.7 is achieved with the pseudo-inverse optimization method.

The wind tunnel investigation demonstrates the potential of real-time drag optimization technology. Several new capabilities are developed that could enable future adaptive wing technologies for flexible wings equipped with drag control devices such as the VCCTEF.

I. Introduction

Air vehicles are typically designed to maintain sufficient structural rigidity for safe load-carrying capacity. Advanced composite materials have gained widespread adoption as materials of choice for modern airframe structures. This adoption is driven by the need to reduce airframe operational empty weight (OEW) which is a major consideration for improving energy efficiency. Composite structures tend to exhibit less structural rigidity while providing the same load-carrying capacity. An example of light-weight airframe design is the Boeing 787 Dreamliner aircraft, which has a more flexible wing structure than older-generation aircraft. This increased structural flexibility afforded by modern materials could be exploited to improve aerodynamic efficiency of future air vehicle concepts.[1]

As the wing flexibility increases, aeroelastic interactions with aerodynamic forces and moments can alter aircraft aerodynamics significantly, thereby degrading aerodynamic efficiency. Increased drag, hence increased fuel burn, is one such potential consequence. Without means for aeroelastic compensation, the benefit of weight reduction afforded by composite materials could be offset by suboptimal aerodynamic performance at off-design flight conditions. Performance Adaptive Aeroelastic Wing (PAAW) technology can potentially address these technical challenges for future flexible wing transports. PAAW technology leverages multi-disciplinary solutions to maximize the aerodynamic performance payoff of future adaptive wing design, while simultaneously addressing operational constraints that can prevent optimal aerodynamic performance from being realized.

To address the performance aspects of wing flexibility in transport design, NASA developed a wing shaping control concept called the variable camber continuous trailing edge flap (VCCTEF) in 2010.[1–3] This study shows that highly flexible wing aerodynamic surfaces can be elastically shaped in-flight by active controls of wing twist and bending to optimize the wing shape for improved aerodynamic efficiency. Subsequently, this study has been further investigated since 2011. Boeing Research and Technology collaborated with NASA under a two-phase study to further develop the VCCTEF concept. The Phase I study was performed during 2012 to refine the initial VCCTEF concept and develop actuation mechanisms.[4,5] The Phase II study was a two-year effort from 2013 to 2014. The objectives of the Phase II study were to conduct aeroelastic analysis and flutter suppression control as well as two wind tunnel experiments to validate the VCCTEF design for cruise and high-lift performance.[6–8]

The VCCTEF system, as shown in Fig. 1, employs a light-weight shaped memory alloy (SMA) technology for actuation and three individual chordwise segments, as shown in Fig. 2, to provide a variable camber aerodynamic surface to shape the chordwise pressure distribution for improved aerodynamic performance. The VCCTEF system is divided into multiple sections attached to the outer wing and the inner wing. Each spanwise flap section has three

cambered flap segments that can be individually commanded. These cambered flaps are joined to the next section by a flexible transition material installed with the same shape as the camber and thus providing a continuous trailing edge flap throughout the wing span with no drag-producing gaps.[5] This continuous trailing edge flap design combined with the flap camber result in lower drag increase during flap deflections. In addition, it also offers a potential noise reduction benefit. This results in the ability to control the wing twist shape as a function of span, resulting in a change to the wing twist to establish the best lift-to-drag ratio (L/D) at any aircraft gross weight or mission segment. Current wing twist on commercial transports is permanently set for one cruise configuration, usually for a 50% loading or mid-point on the gross weight schedule. The VCCTEF offers a mission-adaptive wing capability by enabling a different wing twist setting for each gross weight condition and also different settings for climb, cruise and descent, a major factor in obtaining best L/D conditions.

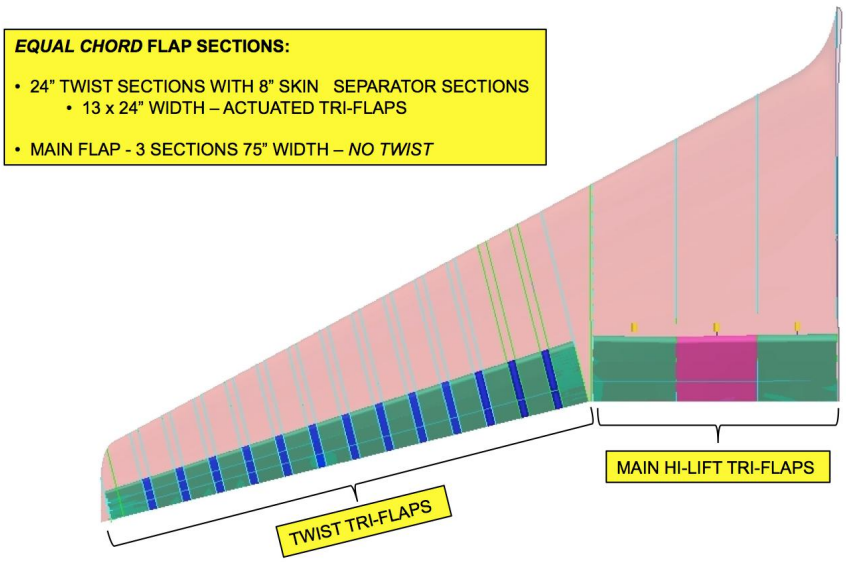

Figure 1. Typical Transport Wing Configured with the Variable Camber Continuous Trailing Edge Flap

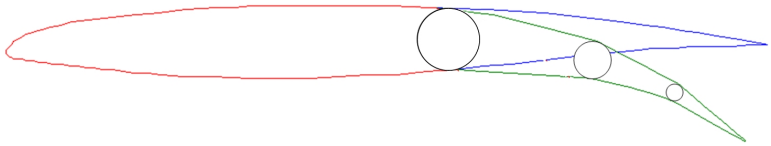

Figure 2. Three-Segment Variable Camber Flap

Adaptive wing technologies such as the VCCTEF are envisioned to provide the ability to automatically reconfigure a wing configuration in-flight to maximize the cruise aerodynamic efficiency. In an ideal setting, an integrated adaptive wing design would incorporate many subsystems including actuation mechanisms, sensors, flight control system, flight management system, and software algorithms. The full potential of adaptive wing technologies can be further realized if these subsystems can be designed synergistically to achieve real-time drag optimization in-flight.

In the current practice, cruise drag optimization in modern transport design is implemented as a table-lookup method for scheduling flap settings as a function of aircraft gross weight, airspeed, and altitude. The table-lookup method generally depends on a validated analytical model of the reference geometry of a particular aircraft design. The analytical model must be validated with wind tunnel and flight test data to ensure the accuracy of the performance prediction. Aircraft production variances, however, can result in varying performance characteristics among aircraft. Different operating conditions such as gross weight, airspeed, and altitude could also contribute to the variability of the aircraft performance. All of these possible variations can result in a wide range of performance characteristics and uncertainty in the table-lookup method.

Real-time drag optimization strategy could hold promise and could provide more flexibility than the table-lookup method. It is perhaps the ultimate goal of the adaptive wing vision to make aircraft 'smarter' and truly mission-adaptive. However, many technical hurdles must be overcome in order to realize this vision. In a larger picture, such a strategy must be able to predict the aerodynamic performance very accurately by estimation using only data from sensors and flap inputs. The sensors themselves must be able to reliably and accurately measure the aerodynamic performance parameters. The performance estimation has to be coupled to the flight control system which sends commands to the flap actuators. The real-time drag optimization must be able to compute in real-time the optimal flap configuration and aircraft states. Then, the outputs from the real-time drag optimization are to be translated into commands to be processed by the aircraft flight control system and or flight management system. This strategy has been examined in a recent study which proposes a real-time model identification technique based on the recursive least-squares method to construct an on-line surrogate aerodynamic model of a flexible wing aircraft.[9] The surrogate aerodynamic model is then used in a gradient optimization to compute the optimal setting of the VCCTEF that minimizes the cruise drag while maintaining the aircraft flight path.

The VCCTEF technology has undergone a series of low-speed wind tunnel tests in the University of Washington Aeronautical Laboratory (UWAL) to validate this technology. To date, three wind tunnel test campaigns have been completed. The first wind tunnel test campaign was conducted in 2013 to assess the aerodynamic performance of the VCCTEF.[10,11] This test shows that up to 6% drag reduction has been observed in the experimental data for the tested VCCTEF configurations. The second wind tunnel test campaign was conducted in 2014 to assess the high-lift performance of the VCCTEF.[12,13] The high-lift wind tunnel model incorporates one variable camber Fowler flap at the inboard as part of the VCCTEF system along with a variable camber Krueger continuous leading edge slat. The test results show that the VCCTEF can achieve the necessary high-lift $C_{L_{max}}$ requirement. The third wind tunnel test campaign was conducted in 2017 and 2018 to validate the real-time drag optimization strategy which is the subject of this paper. A fourth wind tunnel test campaign is currently underway to validate a multi-objective gust load alleviation and drag optimization control technology in 2019.

The real-time drag optimization wind tunnel test is funded by a NASA SBIR Phase II contract with Scientific Systems Company, Inc. (SSCI) and University of Washington (UW) as a sub-contractor. This wind tunnel test comprises three different test entries which took place in the UWAL in 2017 and 2018. Unlike the first two wind tunnel test campaigns, the VCCTEF is actively controlled by servo-actuator mechanisms in the real-time drag optimization wind tunnel test. As a result, the wind tunnel model is a much more complex mechanism than the previous wind tunnel models. The first wind tunnel test entry took place in September 2017. This test revealed major hardware issues and required further redesign of the flap actuators. The second test entry took place in April 2018 when the real-time adaptive drag optimization was first conducted. However, the test objectives were not met due to the issues with the onboard aerodynamic model identification algorithm which incorrectly identified model parameters due to incorrect settings in the software algorithm. As a result, the real-time drag optimization failed to find optimal solutions. The third and final test entry took place in June 2018 after the issues with the onboard aerodynamic model identification algorithm have been identified and corrected. The test objectives were successfully demonstrated this time as the real-time drag optimization was able to identify several optimal solutions.

This paper describes the development of the real-time drag optimization strategy for the wind tunnel experiment, the experimental set-up, and the experimental results.

II. Wind Tunnel Model Description

The wind tunnel model for the real-time drag optimization experiment is a sub-scale model of a Common Research Model (CRM) wing.[14] Comparing to the wing planform of the full-scale CRM wing starting at the side-of-body wing station,[14] the wind tunnel model is a 8.2% sub-scale CRM wing. This CRM wing is designed to have about a wing tip deflection of 10% of the wing semi-span to represent a typical wing flexibility of the current state-of-the-art high aspect ratio wings of modern transport aircraft such as the Boeing 787. The wing is 85 inches in length with a leading edge sweep angle of 35° at the quarter chord. The wing physical parameters are provided in Table 1.

The original CRM wing geometry[14] is a cruise shape outer mold line (OML) with a jig-shape twist to account for the wing aeroelastic deflection at the design cruise condition. Modifications are made to the original CRM wing geometry to account for the increase in the wing flexibility with a 10% wing tip deflection. The cruise shape OML is removed by flattening the original CRM wing geometry. A new jig-shape twist is then applied to the flattened OML. The new jig-shape twist is computed by an aero-structural optimization using the CART3D Euler CFD code coupled to a notional structural beam model of the wing for the design $C_L = 0.5$ at Mach 0.3. The optimized incremental jig-shape twist is shown in Fig. 3. This incremental jig-shape twist is then applied to the original design jig-shape

twist.[14]

Wing Semi-Span	85 inches
Location of Yehudi Break	25.083 inches
Root Chord	38.101 inches
Tip Chord	8.806 inches
Chord at Yehudi Break	23.425 inch
Leading Edge Sweep	37.1818°
Wing Area	12.0608 ft^2
Mean Aerodynamic Chord	23.5221 inches
Aspect Ratio	8.3201

Table 1. CRM Wing Physical Parameters

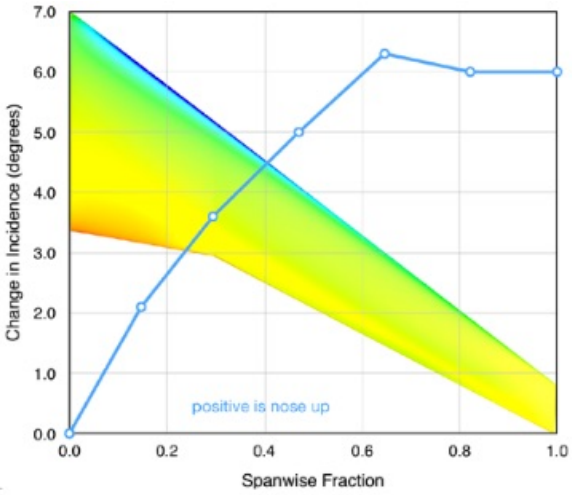

Figure 3. CRM Wing Optimized Incremental Jig-Shape Twist Optimized by CART3D

The wing is constructed using a foam core covered with a two-layer fiberglass skin as shown in Fig. 4. The continuous fiberglass skin construction provides a clean aerodynamic surface for accurate lift and drag measurements and does not follow a common beam / aerodynamic shell design practice for subsonic aeroelastic wind tunnel models. The VCCTEF system comprises six active two-segment control surfaces. These 12 control surfaces are driven by 12 independent servo-actuators for the real-time drag optimization strategy. The flap segments and actuator housing are made of aluminum. The flap gaps are sealed with elastomer transition inserts to provide the continuous trailing edge. The 12 flap segments are numbered from 1 to 6 from inboard to outboard. The inner cambered segment is designated with the letter A and the outer cambered segment is designated with the letter B. The flap numbering is shown in Fig. 5.[15]

The wing is attached to the sidewall balance in the test section in a horizontal position via a steel tube to which the wing is bolted at the load block, as shown in Fig. 5.[15] The sidewall balance provides the lift, drag, and pitching moment measurements. A control system computer is interfaced with the wind tunnel data acquisition system to drive the angle of attack and flap positions during the experiment.

The sidewall balance measures 6 force and moment components. The wind tunnel test only concerns with the lift and drag measurements. To alleviate the boundary layer effect in the test section, the wing is mounted 6 inches off the sidewall through a hole in a non-metric splitter plate, as shown in Fig. 6.[15]

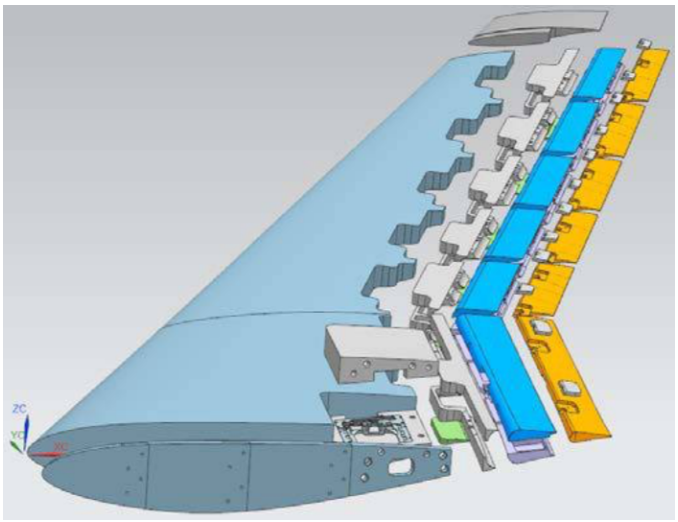

Figure 4. Exploded View of CRM Wing with VCCTEF System

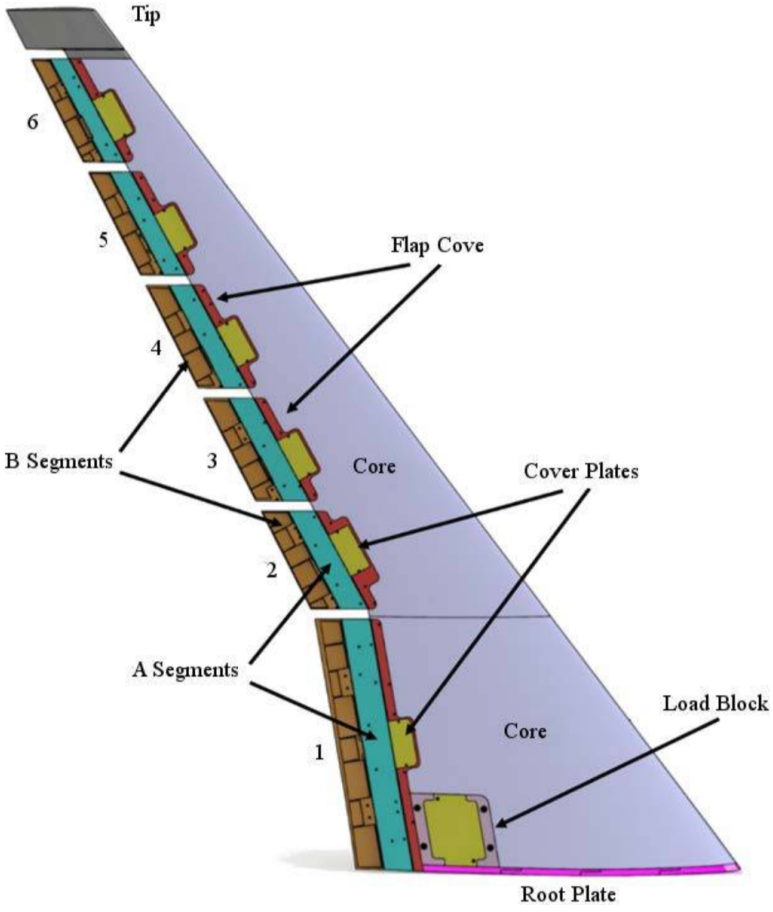

Figure 5. CRM Wing Planform

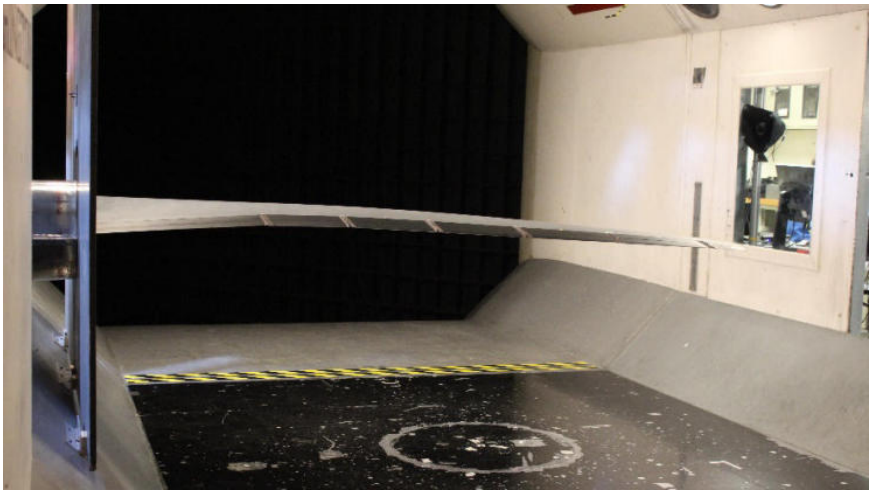

Figure 6. CRM Wing Installed in Test Section (September 2017)

The flap actuators are packaged inside the outer mold line of the wind tunnel model to provide a clean aerodynamic surface with no external protuberances. The requirement for the flap actuators to be able to fit in the small internal flap volumes presents a significant challenge in the design which places limitations on the size and power of the actuators. A typical flap actuator assembly is shown in Figs. 7 and 8. Initially, the actuators selected for the wind tunnel model are Spektrum A7050 thin-wing servos which were used during the first test entry. These servos were modified as linear actuators. However, these servos experienced high load duty cycles during the test which caused cracking in the plastic servo housing. These servos were then replaced with more robustly designed MKS HV6130 servos.[15]

Each actuator is installed in an aluminum cradle, along with an optical encoder sensor to measure the actuator extension. The optical encoders are US Digital EM2 quadrature encoders with differential A and B quadrature. The optical encoders can support a resolution of 0.000125 inches which produces an angular resolution better than 0.1 degrees. In actual practice, the accuracy of the flap position is on the order of 1 degree, and in some cases could be up to 3 degrees. This relative low resolution of the flap position is due largely to the mechanical backlash and the manufacturing tolerances of the flap hinges, as well as the servo lead screw misalignment.[15]

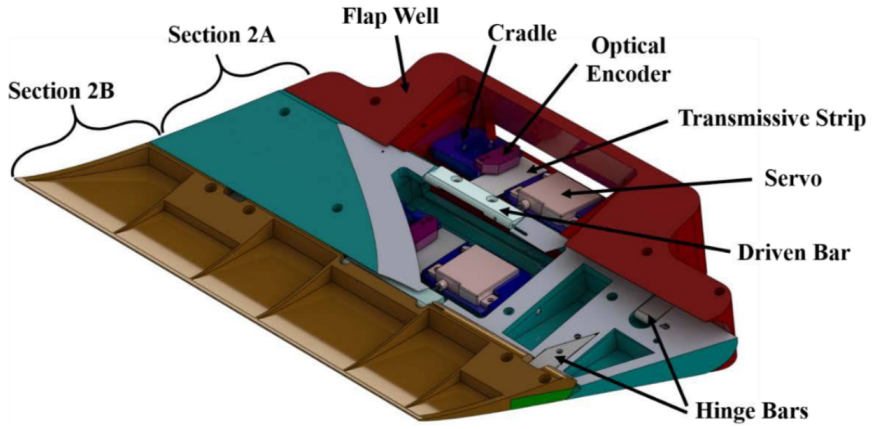

Figure 7. Exploded View of VCCTEF Actuator Assembly of Flaps 2A and 2B

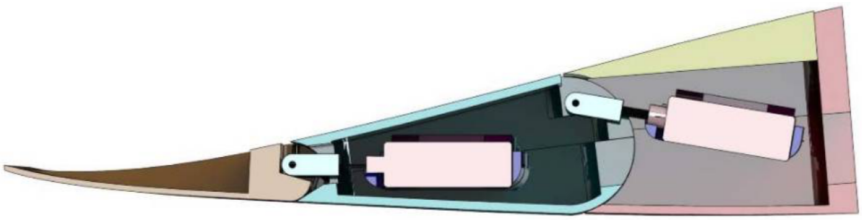

Figure 8. Cutaway View of VCCTEF Actuator Assembly of Flaps 2A and 2B

Initially, the elastomer transition inserts that connect the neighboring flap segments to provide a continuous trailing edge were made of solid silicone rubber. Figure 9 shows the silicone rubber transition inserts being stretched by the flap deflections. During the first test entry, these silicone rubber transition inserts were quite stiff and created too much resistance to the flap motion. These transition inserts were replaced with a new dual-material 3D-printed design with a hollow cross section as shown in Fig. 10. Figure 11 shows a 3D printed transition insert installed on the wing during the second test entry in April 2018.[15]

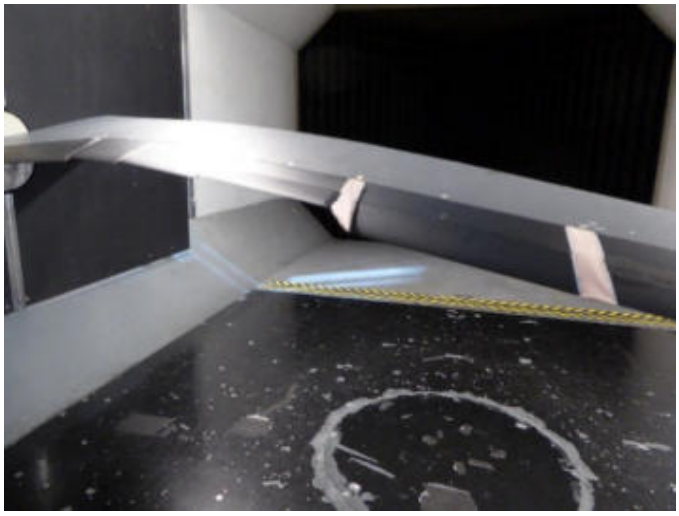

Figure 9. CRM Wing with VCCTEF Silicone Rubber Transition Inserts (September 2017)

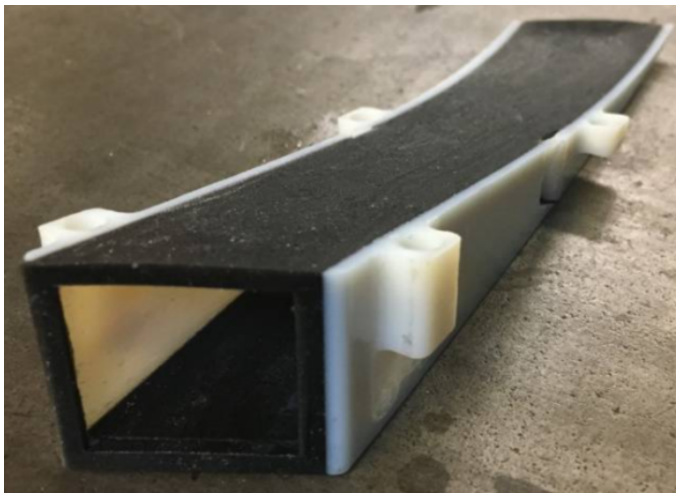

Figure 10. CRM Wing with VCCTEF 3D-Printed Transition Inserts

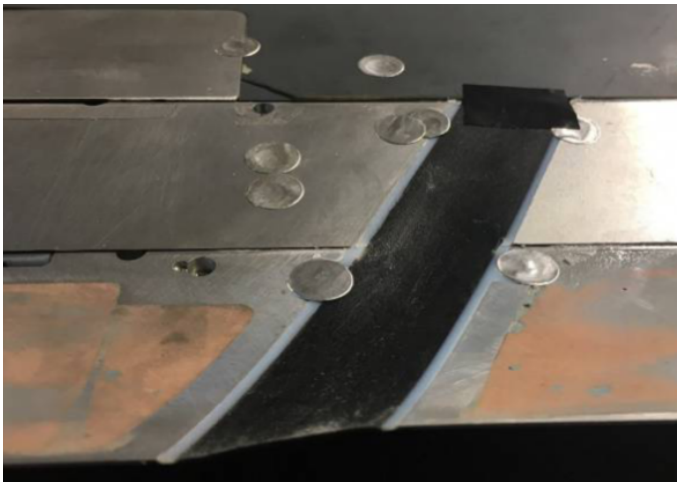

Figure 11. CRM Wing with As-Installed VCCTEF 3D-Printed Transition Inserts (April 2018)

III. VCCTEF Control System

The VCCTEF control system was developed to provide a TCP network interface to the individual servos for each of the flap segments. The control system interfaces with the actuator control via an onboard microcontroller and acts as networked device for the real-time drag optimization algorithm to communicate with. Two microcontrollers are used to close the feedback loop, as shown in the schematic diagram of the control system in Figure 12.[15]

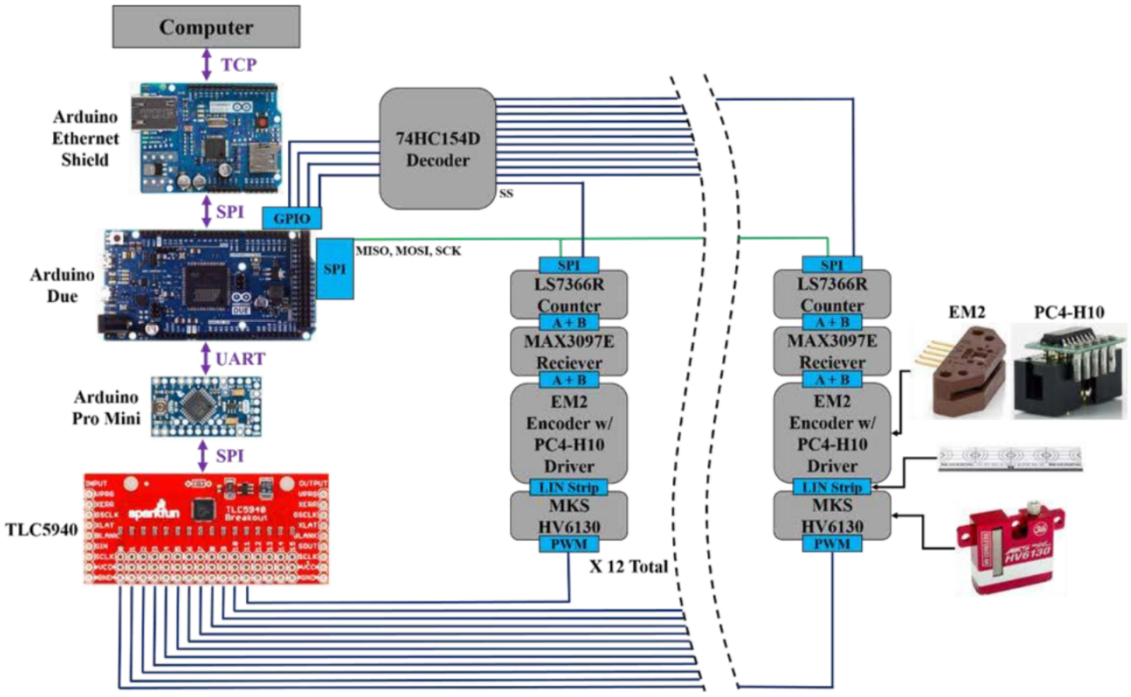

Figure 12. CRM Wing with As-Installed VCCTEF 3D-Printed Transition Inserts (April 2018)

The first microcontroller, an Arduino Pro Mini (ATmega328) located in the flap housing, is tasked with generating pulse-width-modulated (PWM) servo control signals to drive the servos. The Arduino Pro Mini interfaces with a 16-channel TLC5940 PWM driver that supplies the PWM signals to the servos.

The second microcontroller, a 32-bit ARM processor-based microcontroller Arduino Due performs the feedback action on the error signals between the encoder positions and the commanded values to control the flap servos. The

Arduino Due is housed in a separate control box located outside the wind tunnel test section. The quadrature encoders transmit their signals via a differential line driver (US Digital PC4-H10 driver) to the control box. Twelve LS7366R quadrature encoder counter chips convert quadrature encoder signals into counts which are fed to the Arduino Due via Serial-Parallel Interface (SPI).[15]

The control system also interfaces with the wind tunnel data acquisition system which supplies the balance output signals for lift, drag, and pitching moment (not used), as well as the angle of attack signal. The balance output signals are raw signals without any wind tunnel correction for tare and other necessary corrections.

A VICON Nexus 3D motion tracking system with 6 VICON Bonita infrared cameras is used to track the position of the markers on the wing to measure the wind-on wing deflection. These marker locations are shown in Fig. 13.[15]

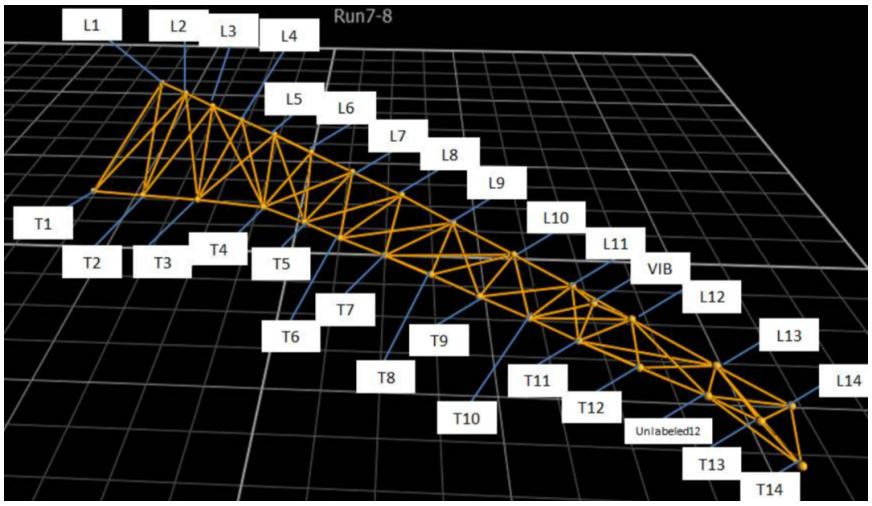

Figure 13. VICON Marker Locations on Wing

IV. Real-Time Drag Optimization Framework

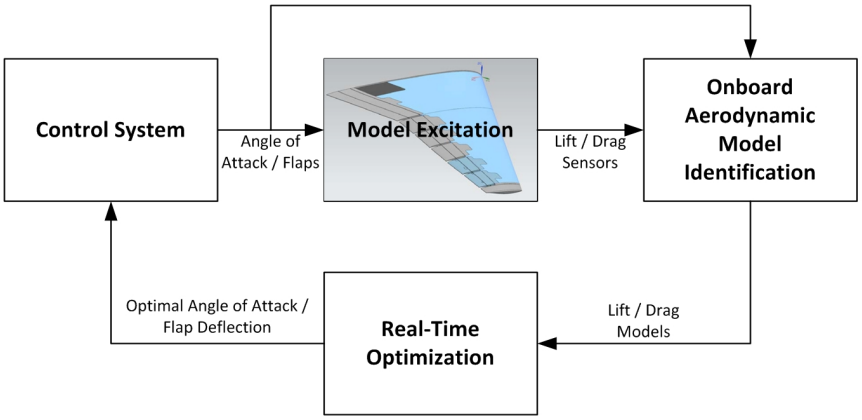

Figure 14. Real-Time Drag Optimization Framework

Figure 14 illustrates the real-time drag optimization framework which comprises a control system, an onboard aerodynamic model identification, a model excitation, and a real-time drag optimization. The control system sends command signals to the wing to change the angle of attack and flap positions. The onboard aerodynamic model identification performs real-time parameter identification to compute the sensitivities of the lift and drag coefficients measured from the sidewall balance with respect to the angle of attack and individual flap positions. These aerodynamic sensitivities are then used to form the onboard aerodynamic model for use in the real-time drag optimization. Both the

onboard aerodynamic model and the identification recursive-least squares (RLS) algorithm were developed by NASA. The model excitation provides an input set of commands of the angle of attack and flap positions. The real-time drag optimization performs the optimization to minimize drag at a target off-design lift coefficient. Several real-time drag optimization algorithms were developed by both SSCI and NASA. SSCI developed a genetic drag optimization algorithm. NASA developed a number of gradient-based optimization algorithms. Both the SSCI and NASA-developed algorithms were tested during the second test entry in April 2018, but only NASA-developed algorithms were tested during the third and final test entry in June 2018.

The details of the onboard aerodynamic model identification, model excitation, and real-time drag optimization are described further as follows.

A. Onboard Aerodynamic Model Identification

The flap positions are defined by a column vector $\delta = \begin{bmatrix} \delta_1 & \dots & \delta_6 & \delta_7 & \dots & \delta_{12} \end{bmatrix}^\top$ where δ_i, $i = 1,\dots,6$ is the position of the $i-$th inner cambered flap segment numbered from inboard to outboard and δ_i, $i = 7,\dots,12$ is the position of the i-th outer or trailing edge cambered flap segment numbered from inboard to outboard. The 12 individual flap segments can be commanded independently or in a prescribed camber. A circular arc camber can be commanded using only $\frac{1}{n_{camber}}$ of the number of flap segments where n_{camber} is the number of chordwise cambered segments, in a manner such that the positions of the inner cambered flap segments are scheduled in proportion to the positions of the outer cambered flap segments by the following relationship:

$$\delta_{i+\frac{n_{flap}(j-1)}{n_{camber}}} = \frac{j}{n_{camber}} \delta_{i+\frac{n_{flap}j}{n_{camber}}} \tag{1}$$

where $i = 1,\dots,,\frac{n_{flap}}{n_{camber}}$, $j = 1,\dots,n_{camber}-1$, and n_{flap} is the total number of flap segments. Thus, for a two-cambered segment VCCTEF configuration, the positions of the inner cambered flap segments are prescribed by the commanded positions of the outer cambered flap segments as

$$\delta_i = \frac{\delta_{i+6}}{2} \tag{2}$$

where $i = 1,\dots,6$.

The parabolic arc camber can offer a better drag reduction effectiveness than the circular arc camber as found in a recent study.[16] A general parabolic arc camber is described by

$$\delta_{i+\frac{n_{flap}(j-1)}{n_{camber}}} = \frac{\sum_{k=1}^{j} k}{\sum_{k=1}^{n_{camber}} k} \delta_{i+\frac{n_{flap}j}{n_{camber}}} \tag{3}$$

Thus, for a two-cambered segment VCCTEF configuration, the positions of the inner flap segments are prescribed by

$$\delta_i = \frac{\delta_{i+6}}{3} \tag{4}$$

1. *Lift Coefficient Models*

Two lift coefficient models are used in the real-time drag optimization to enforce the lift constraint in the real-time drag optimization. They are described as follows.

1. Linear Lift Coefficient Model: This is the simplest model which describes the lift coefficient as

$$C_L = C_{L_0} + C_{L_\alpha}\alpha + C_{L_\delta}\delta \tag{5}$$

   This linear lift coefficient model is adequate when the lift curve is reasonably linear. However, in cases where the lift curve is nonlinear due to flow separation or flow at low Reynolds number, then a high-order lift coefficient model may become necessary. This turns out to be the case in the wind tunnel test.

2. Quadratic Lift Coefficient Model: A quadratic lift coefficient model describes the quadratic relationship between the lift coefficient and the angle of attack. It is used to capture the nonlinearity between the lift coefficient and the angle of attack due to early stall characteristics at low Reynolds number as seen in the wind tunnel test.

The quadratic lift coefficient model still employs a linear model for the flap positions in order to simplify the real-time drag optimization strategy. The quadratic lift coefficient model is described by

$$C_L = C_{L_0} + \sum_{l=1}^{2} C_{L_{\alpha^l}} \alpha^l + C_{L_\delta} \delta \tag{6}$$

2. Drag Coefficient Models

The real-time drag optimization employs two drag coefficient models. These models are:

1. Quadratic Drag Coefficient Model: This is the simplest model which describes the drag coefficient as

$$C_D = C_{D_0} + C_{D_\alpha} \alpha + C_{D_\delta} \delta + C_{D_{\alpha^2}} \alpha^2 + C_{D_{\alpha\delta}} \alpha\delta + \delta^\top C_{D_{\delta^2}} \delta \tag{7}$$

Initially, the full quadratic drag coefficient model is used during the first test entry. Later on, two assumptions are made in order to simplify the onboard aerodynamic model identification recursive least-squares algorithm. The cross term drag sensitivity vector $C_{D_{\alpha\delta}}$ is assumed to be small and therefore can be neglected. The quadratic drag sensitivity matrix $C_{D_{\delta^2}}$ is assumed to be a strictly diagonal matrix with all off-diagonal terms assumed to be negligible. The off-diagonal terms are found to be difficult to estimate accurately by the model identification recursive least-squares algorithm. Moreover, by retaining only the diagonal terms, the number of parameters for the matrix $C_{D_{\delta^2}}$ is substantially reduced from 72 to 12 if all the 12 flap segments are used in the real-time drag optimization strategy, thus resulting in substantial time savings for the onboard aerodynamic model identification. Furthermore, the elimination of the off-diagonal terms simplifies considerably the assurance of positive definiteness of the matrix $C_{D_{\delta^2}}$ by only ensuring that all the diagonal terms are positive-valued. This positive definiteness ensures that the real-time drag optimization strategy can produce feasible solutions. Thus, the simplified quadratic drag coefficient model can be expressed as

$$C_D = C_{D_0} + C_{D_\alpha} \alpha + C_{D_\delta} \delta + C_{D_{\alpha^2}} \alpha^2 + \delta^\top C_{D_{\delta^2}} \delta \tag{8}$$

2. Higher-Order Drag Coefficient Model: Further increase in the accuracy in the drag coefficient estimation apparently becomes necessary during the wind tunnel test since the measured drag coefficient does not follow the quadratic relationship well as the angle of attack increases beyond a certain limit. Thus, a higher-order drag coefficient model up to 6^{th}-order is used during the last test entry in June 2018. This model is described by

$$C_D = C_{D_0} + \sum_{m=1}^{6} C_{D_{\alpha^m}} \alpha^m + C_{D_\delta} \delta + \delta^\top C_{D_{\delta^2}} \delta \tag{9}$$

The onboard aerodynamic model identification process employs a recursive least-squares (RLS) algorithm to estimate the unknown parameters in the onboard aerodynamic model. In addition, a batch least-squares (BLS) algorithm is employed during the final test entry in June 2018.

The lift coefficient model can be represented in general as

$$C_L(\alpha, \delta) = \Theta_L^\top \Phi_L(\alpha, \delta) \tag{10}$$

where $\Theta_L = \begin{bmatrix} C_{L_0} & C_{L_\alpha} & C_{L_\delta} & C_{L_{\alpha^2}} \end{bmatrix}^\top$ is a column vector of the unknown lift coefficient model parameters corresponding to the input column vector $\Phi_L(\alpha, \delta) = \begin{bmatrix} 1 & \alpha & \delta^\top & \alpha^2 \end{bmatrix}^\top$.

The drag coefficient model can be expressed in general as

$$C_D(\alpha, \delta) = \Theta_D^\top \Phi_D(\alpha, \delta) \tag{11}$$

where $\Theta_D = \begin{bmatrix} C_{D_0} & C_{D_\alpha} & C_{D_\delta} & C_{D_{\alpha^2}} & \text{diag}\left(C_{D_{\delta^2}}\right) & C_{D_{\alpha^3}} & \dots & C_{D_{\alpha^6}} \end{bmatrix}^\top$ is a column vector of the unknown drag coefficient model parameters corresponding to the input column vector $\Phi_D(\alpha, \delta) = \begin{bmatrix} 1 & \alpha & \delta^\top & \alpha^2 & \delta^{2\top} & \alpha^3 & \dots & \alpha^6 \end{bmatrix}^\top$ where $\delta^2 = \begin{bmatrix} \delta_1^2 & \dots & \delta_6^2 & \delta_7^2 & \dots & \delta_{12}^2 \end{bmatrix}^\top$ or $\delta^2 = \begin{bmatrix} \delta_7^2 & \dots & \delta_{12}^2 \end{bmatrix}^\top$ if a prescribed camber is used and $\text{diag}\left(C_{D_{\delta^2}}\right)$ is a row vector of the diagonal elements of $C_{D_{\delta^2}}$.

The onboard aerodynamic model identification process uses the input data which comprise the angle of attack and the flap positions and the output data which comprise the measured lift and drag coefficients to compute the estimates of the unknown model parameters $\hat{\Theta}_L$ and $\hat{\Theta}_D$. Once the parameter estimates converge, then the real-time optimization is conducted to find an optimal solution.

3. Recursive Least-Squares Method

The recursive least-squares (RLS) method estimates and updates the unknown model parameters at every i-th data point by the following update law:

$$\hat{\Theta}_i = \hat{\Theta}_{i-1} + K_i \left(y_i^\top - \Phi_i^\top \hat{\Theta}_{i-1} \right) \tag{12}$$

where $\Theta_i = \Theta_{L,i}$ or $\Theta_i = \Theta_{D,i}$, $y_i = C_{L,i}$ or $y_i = C_{D,i}$, $\Phi_i = \Phi_{L,i}$ or $\Phi_i = \Phi_{D,i}$, and K_i is given by

$$K_i = \frac{R_{i-1}\Phi_i}{\beta + \Phi_i^\top R_{i-1}\Phi_i} \tag{13}$$

where $\beta > 0$ is a constant usually set to 1 and $R_i > 0$ is the covariance matrix with the following update law:

$$R_i = \frac{1}{\lambda}\left[I - R_{i-1}\left(\frac{\Phi_i \Phi_i^\top}{\beta + \Phi_i^\top R_{i-1}\Phi_i} \right) \right] R_{i-1} \tag{14}$$

and λ is a forgetting factor which is usually set to 1 but can be adjusted for time-varying noise conditions.

4. Batch Least-Squares Method

The batch least-squares (BLS) method estimates and updates the unknown model parameters after a specified number of data points has been acquired. It is given by the following update law:

$$\hat{\Theta} = A^{-1} B \tag{15}$$

where

$$A = \sum_{i=1}^{N} \Phi_i \Phi_i^\top \tag{16}$$

$$B = \sum_{i=1}^{N} \Phi_i y_i^\top \tag{17}$$

To ensure the model parameter convergence, the input data set has to be sufficiently rich and contain uncorrelated signals. This condition is referred to as the persistent excitation condition which is mathematically expressed by the inequality

$$\sum_{i=1}^{N} \Phi_i \Phi_i^\top \geq \gamma I \tag{18}$$

where $\gamma > 0$ and I is the identity matrix. The input data set that contains values of the angle of attack and flap positions, therefore, must be designed in order to provide enough excitation to ensure sufficient model parameter convergence.

B. Model Excitation

The real-time drag optimization process begins with a model excitation whereby the wing is excited by the control input signals generated by the commanded angle of attack and flap positions. A number of model excitation strategies are developed. These are described as follows.

1. Random Excitation Method

The default model excitation strategy is to excite the wing with a full input set that contains sufficient number of data points which specify the commands of the angle of attack and flap positions. Since there are 13 control input variables, if each input variable is to be specified over a pre-determined range of values by n randomly generated data points, the number of permutations can be very large and could present a computational challenge if the data acquisition is not sufficiently fast. Therefore, this strategy is generally computationally intensive and can take a long time to achieve model parameter convergence during the wind tunnel test.

2. *Sweep Method*

The sweep method is a two-stage model excitation method that includes an initial sweep and a directed sweep. It provides some computational efficiency over the random excitation method. The initial sweep is designed to provide the model excitation to identify the lift coefficient model during the initial stage of the onboard aerodynamic model identification as shown in Fig. 15.

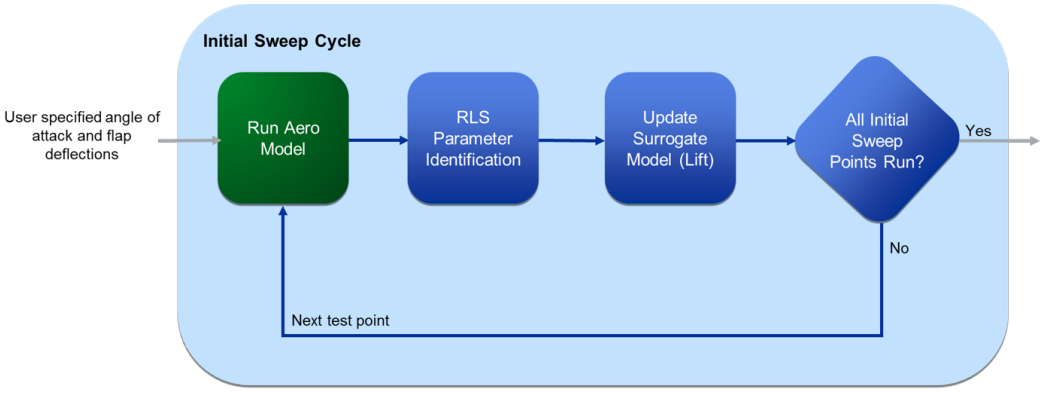

Figure 15. Initial Sweep Cycle

The data points in the input set during the initial sweep contain both the commanded angles of attack and the flap positions which can be specified a priori during the initialization of the algorithm. Because only the lift coefficient model is to be identified during the initial sweep, the input set can be reduced in size to increase the computational efficiency. After the initial sweep is completed and the lift coefficient model is identified, the estimated angle of attack $\hat{\alpha}$ is computed from the estimated lift coefficient model using the linear lift coefficient model to match the target off-design lift coefficient C_L^* as

$$\hat{\alpha} = \frac{C_L^* - \hat{C}_{L_0} - \hat{C}_{L_\delta}\delta}{\hat{C}_{L_\alpha}} \tag{19}$$

where the hat symbol denotes the model parameter estimates.

The flap positions are initially assumed to be at some values such as zero in order to estimate the angle of attack. The wing is then commanded to move to the new angle of attack $\alpha = \hat{\alpha}$. A directed sweep is performed next to identify the drag coefficient model as shown in Fig. 16. The input set now contains only the flap positions while the angle of attack is held constant during the directed sweep. The quadratic drag coefficient model used in the directed sweep therefore becomes a function of the flap positions only and is given by

$$C_D = C_{D_0}^* + C_{D_\delta^*}\delta + \delta^\top C_{D_{\delta 2}}^* \delta \tag{20}$$

where the asterisk denotes different quantities than those in Eq. (8).

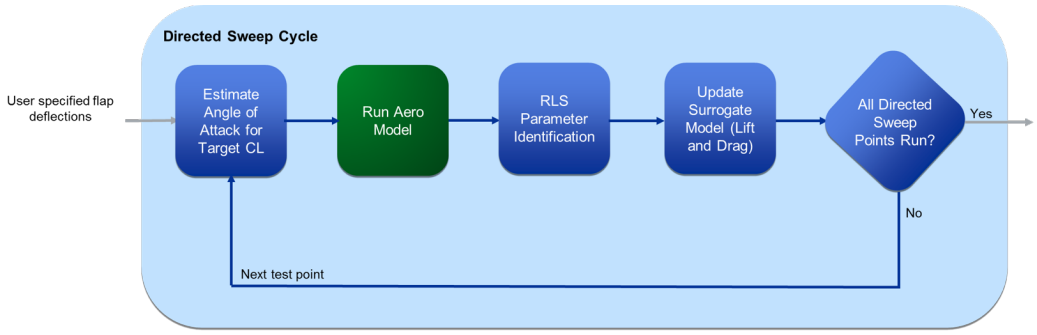

Figure 16. Initial Sweep Cycle

The onboard aerodynamic model identification is then revised with the drag coefficient model as

$$C_D(\delta) = \Theta_D^\top \Phi_D(\delta) \tag{21}$$

where $\Theta_D = \begin{bmatrix} C^*_{D_0} & C^*_{D_\delta} & \text{diag}\left(C^*_{D_{\delta^2}}\right) \end{bmatrix}^\top$ is a column vector of the unknown drag coefficient model parameters corresponding to the input column vector $\Phi_D(\delta) = \begin{bmatrix} 1 & \delta^\top & \delta^{2\top} \end{bmatrix}^\top$.

Once the drag coefficient model is identified, the real-time optimization process is performed to compute the estimated optimal flap position vector $\hat{\delta}$. This set of the newly computed flap positions is then used to update the estimated angle of attack $\hat{\alpha}$. The process is then repeated until the estimated angle of attack converges the optimal angle of attack. The sweep method was not exercised during the wind tunnel test due to the issues encountered with the hardware and software during the first two test entries.

3. Iterative Angle-of-Attack Seeking Method

This model excitation method is proposed during the third entry as an alternative method to both the other model excitation methods to speed up the real-time optimization process. The method decouples the estimation of the model parameters that involves the angle of attack from the estimation of the model parameters that involve the flap positions. The method begins with a clean wing angle-of-attack sweep at zero flap deflections. The lift and drag coefficient models for the clean wing configuration are given by

$$\bar{C}_L = C_{L_0} + \sum_{l=1}^{2} C_{L_{\alpha^l}} \alpha^l \tag{22}$$

$$\bar{C}_D = C_{D_0} + \sum_{m=1}^{6} C_{D_{\alpha^m}} \alpha^m \tag{23}$$

where $\bar{C}_L$ and $\bar{C}_D$ are the clean wing lift and drag coefficients at the initial angle of attack.

Then, the onboard aerodynamic model identification is applied to the input set which contains only the commanded angles of attack while the flap positions are held fixed at zero. This input set can contain only a few angles of attack. Therefore, a significant time saving can be achieved. The model parameters C_{L_0}, $C_{L_{\alpha^l}}$, C_{D_0}, and $C_{D_{\alpha^m}}$ can be estimated with reasonable accuracy with a well-chosen input set of the commanded angles of attack. The onboard aerodynamic model identification is then revised with simpler lift drag coefficient models as

$$\bar{C}_L(\alpha) = \Theta_L^\top \Phi_L(\alpha) \tag{24}$$

$$\bar{C}_D(\alpha) = \Theta_D^\top \Phi_D(\alpha) \tag{25}$$

where $\Theta_L = \begin{bmatrix} C_{L_0} & C_{L_\alpha} & C_{L_{\alpha^2}} \end{bmatrix}^\top$ is a column vector of the unknown lift coefficient model parameters corresponding to the input column vector $\Phi_L(\alpha) = \begin{bmatrix} 1 & \alpha & \alpha^2 \end{bmatrix}^\top$ and $\Theta_D = \begin{bmatrix} C_{D_0} & C_{D_\alpha} & \dots & C_{D_{\alpha^6}} \end{bmatrix}^\top$ is a column vector of the unknown drag coefficient model parameters corresponding to the input column vector $\Phi_D(\alpha) = \begin{bmatrix} 1 & \alpha & \dots & \alpha^6 \end{bmatrix}^\top$.

To meet the target off-design lift coefficient C^*_L, the clean wing angle of attack $\bar{\alpha}$ corresponding to C^*_L is estimated as

$$\hat{\bar{\alpha}} = \frac{-\hat{C}_{L_\alpha} + \sqrt{\hat{C}^2_{L_\alpha} + 4\hat{C}_{L_{\alpha^2}}\left(C^*_L - \hat{C}_{L_0}\right)}}{2\hat{C}_{L_{\alpha^2}}} \tag{26}$$

An angle-of-attack command is then issued to move the wing to an initial angle of attack lower than $\hat{\bar{\alpha}}$ since the drag-optimal angle of attack should be less than the clean wing angle of attack with the flap segments in the positive positions which generally create favorable aerodynamics. Once the wing is at the initial angle of attack α, a series of flap position commands are issued to move each of the 12 flap segments, or 6 flap segments if a prescribed camber is used, one at a time while the other flap segments are held fixed through a range of the flap positions contained in the input set. Each of the flap positions contributes incrementally to the lift and drag coefficients as follows:

$$\Delta C_{L_i} = C_{L_i} - \bar{C}_L = C_{L_{\delta_i}} \delta_i \tag{27}$$

$$\Delta C_{D_i} = C_{D_i} - \bar{C}_D = C_{D_{\delta_i}} \delta_i + C_{D_{\delta_i^2}} \delta_i^2 \tag{28}$$

The model parameters $C_{L_{\delta_i}}$, $C_{D_{\delta_i}}$, and $C_{D_{\delta_i^2}}$ are then computed from this input set for the flap positions. The onboard aerodynamic model identification is revised with the incremental lift and drag coefficient models for the individual flap segments as

$$\Delta C_{L_i}(\delta_i) = \Theta_{L_i}\Phi_{L_i}(\delta_i) \tag{29}$$

$$\Delta C_{D_i}(\delta_i) = \Theta_{D_i}^{\top}\Phi_{D_i}(\delta_i) \tag{30}$$

where $\Theta_{L_i} = C_{L_{\delta_i}}$ is an unknown lift coefficient model parameter corresponding to the input $\Phi_{L_i}(\delta_i) = \delta_i$ and $\Theta_{D_i} = \begin{bmatrix} C_{D_{\delta_i}} & C_{D_{\delta_i^2}} \end{bmatrix}^{\top}$ is a column vector of the unknown drag coefficient model parameters corresponding to the input column vector $\Phi_{D_i}(\delta_i) = \begin{bmatrix} \delta_i & \delta_i^2 \end{bmatrix}^{\top}$.

Once the model parameters are estimated, a real-time drag optimization algorithm is used to compute the candidate optimal angle of attack and flap positions. The wing is then commanded to the new angle of attack and flap positions. Each of the flap segments is then commanded to move one by one through the specified range of flap positions in the input set. A new optimal solution of the angle of attack and flap positions is computed and the process is repeated until the solution converges.

C. Real-Time Drag Optimization

Both SSCI and NASA developed the real-time drag optimization algorithms for the wind tunnel test. However, only NASA optimization algorithms were successfully tested during the final test entry in June 2018. The SSCI genetic algorithm was only tested during the second test entry in April 2018 along with NASA second-order gradient Newton-Raphson optimization algorithm both of which were not successful due to the issues with the onboard aerodynamic model identification RLS algorithm.

Once the onboard aerodynamic model identification is complete and returns with a set of estimated model parameters, the real-time optimization process begins. Two algorithms are used: SSCI genetic algorithm which is proprietary and NASA gradient optimization algorithms. The details of the gradient optimization algorithms are discussed in the following section. NASA develops several optimization algorithms for the wind tunnel test. These algorithms are discusses in the following sections.

1. Second-Order Gradient Newton-Raphson Optimization Method

The second-order gradient Newton-Raphson optimization method is the baseline method implemented. The drag optimization problem is formulated as

$$\min_{\alpha,\delta} J = \min_{\alpha,\delta} C_D \tag{31}$$

subject to the lift coefficient constraint $C_L = C_L^*$ where, for the general nonlinear lift and drag coefficient models,

$$C_L = C_{L_0} + \sum_{l=1}^{2} C_{L_{\alpha^l}}\alpha^l + C_{L_\delta}\delta \tag{32}$$

$$C_D = C_{D_0} + \sum_{m=1}^{6} C_{D_{\alpha^m}}\alpha^m + C_{D_\delta}\delta + C_{D_{\alpha\delta}}\alpha\delta + \delta^{\top}C_{D_{\delta^2}}\delta \tag{33}$$

The angle of attack then is solved from the nonlinear lift coefficient model as a function of the flap positions as

$$\alpha(\delta) = \frac{-C_{L_\alpha} + \sqrt{C_{L_\alpha}^2 + 4C_{L_{\alpha^2}}\left(C_L^* - C_{L_0} - C_{L_\delta}\delta\right)}}{2C_{L_{\alpha^2}}} \tag{34}$$

The gradient of the cost function with respect to the flap positions is evaluated as

$$\nabla_\delta J = \left(\frac{\partial C_D}{\partial \delta}\right)^{\top} = \sum_{m=1}^{6} mC_{D_{\alpha^m}}\alpha^{m-1}\left(\frac{\partial \alpha}{\partial \delta}\right)^{\top} + C_{D_\delta}^{\top} + 2C_{D_{\delta^2}}\delta \tag{35}$$

where $\frac{\partial \alpha}{\partial \delta}$ is evaluated from the quadratic lift coefficient model as

$$\frac{\partial \alpha}{\partial \delta} = -\frac{C_{L_\delta}}{\sum_{l=1}^{2} lC_{L_{\alpha^l}}\alpha^{l-1}} \tag{36}$$

This yields

$$\nabla_\delta J = C_{D_\delta}^\top + 2C_{D_{\delta^2}}\delta - C_{L_\delta}^\top \frac{\sum_{m=1}^{6} mC_{D_{\alpha^m}}\alpha^{m-1}}{\sum_{l=1}^{2} lC_{L_{\alpha^l}}\alpha^{l-1}} \tag{37}$$

The Hessian or second partial derivative of the cost function with respect to the flap positions is evaluated as

$$\begin{aligned}\nabla_\delta^2 J &= \frac{\partial \nabla_\delta J}{\partial \delta} \\ &= 2C_{D_{\delta^2}} - C_{L_\delta}^\top \frac{\sum_{m=1}^{5} m(m-1)C_{D_{\alpha^m}}\alpha^{m-2}\frac{\partial\alpha}{\partial\delta}}{\sum_{l=1}^{2} lC_{L_{\alpha^l}}\alpha^{l-1}} + C_{L_\delta}^\top \frac{\sum_{m=1}^{6} mC_{D_{\alpha^m}}\alpha^{m-1}\sum_{l=1}^{1} l(l-1)C_{L_{\alpha^l}}\alpha^{l-2}\frac{\partial\alpha}{\partial\delta}}{\left(\sum_{l=1}^{2} lC_{L_{\alpha^l}}\alpha^{l-1}\right)^2}\end{aligned} \tag{38}$$

The Hessian is then expressed in general as

$$\nabla_\delta^2 J = 2C_{D_{\delta^2}} + \frac{C_{L_\delta}^\top C_{L_\delta}}{\left(\frac{\partial C_L}{\partial\alpha}\right)^3}\left(\frac{\partial^2 C_D}{\partial\alpha^2}\frac{\partial C_L}{\partial\alpha} - \frac{\partial C_D}{\partial\alpha}\frac{\partial^2 C_L}{\partial\alpha^2}\right) \tag{39}$$

where

$$\frac{\partial C_L}{\partial\alpha} = \sum_{l=1}^{2} lC_{L_{\alpha^l}}\alpha^{l-1} \tag{40}$$

$$\frac{\partial^2 C_L}{\partial\alpha^2} = \sum_{l=1}^{1} l(l-1)C_{L_{\alpha^l}}\alpha^{l-2} \tag{41}$$

$$\frac{\partial C_D}{\partial\alpha} = \sum_{m=1}^{6} mC_{D_{\alpha^m}}\alpha^{m-1} \tag{42}$$

$$\frac{\partial^2 C_D}{\partial\alpha^2} = \sum_{m=1}^{5} m(m-1)C_{D_{\alpha^m}}\alpha^{m-2} \tag{43}$$

In order to ensure that the drag optimization attains a local minimum, the Hessian is required to be a positive definite matrix. That is

$$\nabla_\delta^2 J > 0 \tag{44}$$

Since $C_{D_{\delta^2}} >$ and $C_{L_\delta}^\top C_{L_\delta} > 0$, it is required that $\frac{\partial^2 C_D}{\partial\alpha^2}\frac{\partial C_L}{\partial\alpha} > \frac{\partial C_D}{\partial\alpha}\frac{\partial^2 C_L}{\partial\alpha^2}$. For the linear lift coefficient model and quadratic drag coefficient model, this condition is identically satisfied since $\frac{\partial^2 C_D}{\partial\alpha^2}\frac{\partial C_L}{\partial\alpha} = 2C_{D_{\alpha^2}}C_{L_\alpha} > 0 = \frac{\partial C_D}{\partial\alpha}\frac{\partial^2 C_L}{\partial\alpha^2}$. The Hessian for the linear lift coefficient model and quadratic drag coefficient model then becomes

$$\nabla_\delta^2 J = 2C_{D_{\delta^2}}\left(I + \frac{C_{L_\delta}^\top C_{L_\delta}}{C_{L_\alpha}^2}\right) \tag{45}$$

The second-order Newton-Raphson optimization method is described by the following update law:

$$\delta_{i+1} = \delta_i - \left(\nabla_\delta^2 J\right)^{-1}\nabla_\delta J \tag{46}$$

It s is noted that a much simpler expression of $\nabla_\delta^2 J = 2C_{D_{\delta^2}}$ could be used. This would prevent any inaccurate estimation of model parameters that could cause $\nabla_\delta^2 J$ to be non-positive definite which would result in incorrect optimal flap positions. The method is initialized with an initial guess of the flap positions. Then, the angle of attack is computed from Eqs. (34). The flap positions are then updated by the update law in Eq. (46). The process is repeated until the solution converges to the optimal solution when $\nabla_\delta J \approx 0$.

2. Iterative Gradient Optimization Method

The iterative gradient optimization avoids the evaluation of the Hessian which can be inaccurate for the general non-linear lift coefficient and drag coefficient models. The optimization problem is cast an adjoint optimization method by augmenting the cost function with an adjoint variable λ multiplied by the lift coefficient constraint as

$$J = C_{D_0} + \sum_{m=1}^{6} C_{D_{\alpha^m}} \alpha^m + C_{D_\delta} \delta + \delta^\top C_{D_{\delta^2}} \delta + \lambda \left(C_L^* - C_{L_0} - \sum_{l=1}^{2} C_{L_{\alpha^l}} \alpha^l - C_{L_\delta} \delta \right) \tag{47}$$

The gradients of the cost function with respect to the angle of attack, flap positions, and adjoint variable are evaluated as

$$\nabla_\alpha J = \frac{\partial J}{\partial \alpha} = \sum_{m=1}^{6} m C_{D_{\alpha^m}} \alpha^{m-1} - \lambda \sum_{l=1}^{2} l C_{L_{\alpha^l}} \alpha^{l-1} = 0 \tag{48}$$

$$\nabla_\delta J = \left(\frac{\partial C_D}{\partial \delta} \right)^\top = C_{D_\delta}^\top + 2 C_{D_{\delta^2}} \delta - \lambda C_{L_\delta}^\top = 0 \tag{49}$$

$$\nabla_\lambda J = \frac{\partial J}{\partial \lambda} = C_L^* - C_{L_0} - \sum_{l=1}^{2} C_{L_{\alpha^l}} \alpha^l - C_{L_\delta} \delta = 0 \tag{50}$$

These gradients must vanish at the local minimum. Solving for λ from $\nabla_\alpha J$ yields

$$\lambda = \frac{\sum_{m=1}^{6} m C_{D_{\alpha^m}} \alpha^{m-1}}{\sum_{l=1}^{2} l C_{L_{\alpha^l}} \alpha^{l-1}} \tag{51}$$

Substituting λ into $\nabla_\delta J$ yields

$$\nabla_\delta J = C_{D_\delta}^\top + 2 C_{D_{\delta^2}} \delta - C_{L_\delta}^\top \frac{\sum_{m=1}^{6} m C_{D_{\alpha^m}} \alpha^{m-1}}{\sum_{l=1}^{2} l C_{L_{\alpha^l}} \alpha^{l-1}} = 0 \tag{52}$$

Solving for α from $\nabla_\lambda J$ yields

$$\alpha^* = \frac{-C_{L_\alpha} + \sqrt{C_{L_\alpha}^2 - 4 C_{L_{\alpha^2}} \left(C_{L_0} + C_{L_\delta} \delta^* - C_L^* \right)}}{2 C_{L_{\alpha^2}}} \tag{53}$$

Both Eqs. (52) and (53) must be solved simultaneously. An iterative solution can be implemented. An initial guess of the optimal angle of attack $\alpha = \alpha^*$ is made. Then, the optimal flap position vector δ^* is computed from Eq. (52) as

$$\delta^* = \frac{1}{2} C_{D_{\delta^2}}^{-1} \left(-C_{D_\delta}^\top + C_{L_\delta}^\top \frac{\sum_{m=1}^{6} m C_{D_{\alpha^m}} \alpha^{*m-1}}{\sum_{l=1}^{2} l C_{L_{\alpha^l}} \alpha^{*l-1}} \right) \tag{54}$$

Then, α^* is updated from Eq. (53) with the newly computed δ^*. The process is repeated until the solution converges. It should be noted that the iterative gradient optimization process is not coupled to the motion of the wind tunnel model. That is, the wing is not commanded to the iterative values of α^* and δ^* while the iterative gradient optimization algorithm is being computed.

3. Pseudo-Inverse Optimization Method

The pseudo-inverse optimization method was developed for the final test entry and is found to be a simple yet effective method for real-time drag optimization. Consider an optimization problem which seeks to minimize the incremental lift coefficient at the optimal angle of attack α^* as computed by the optimization algorithms. This is expressed as

$$\Delta C_L = C_L^* - C_L(\alpha^*, \delta) = C_L^* - C_{L_0} - \sum_{l=1}^{2} C_{L_{\alpha^l}} \alpha^{*l} - C_{L_\delta} \delta \tag{55}$$

Then, the cost function is formulated as

$$\min_\delta J = \Delta C_L^2 \tag{56}$$

The gradient of the cost function with respect to the flap positions is evaluated as

$$\nabla_\delta J = \left(\frac{\partial J}{\partial \delta}\right)^\top = -2C_{L_\delta}^\top \left(C_L^* - C_{L_0} - \sum_{l=1}^{2} C_{L_{\alpha^l}} \alpha^{*l} - C_{L_\delta}\delta\right) \tag{57}$$

$\nabla_\delta J$ which must vanish at the local minimum can also be expressed as

$$\nabla_\delta J = -2C_{L_\delta}^\top \left[\left(C_L^* - C_{L_0} - \sum_{l=1}^{2} C_{L_{\alpha^l}} \alpha^{*l}\right) \underbrace{C_{L_\delta} C_{L_\delta}^\top \left(C_{L_\delta} C_{L_\delta}^\top\right)^{-1}}_{1} - C_{L_\delta}\delta\right] = 0 \tag{58}$$

Factoring out C_{L_δ} yields

$$-2C_{L_\delta}^\top C_{L_\delta} \left[\left(C_L^* - C_{L_0} - \sum_{l=1}^{2} C_{L_{\alpha^l}} \alpha^{*l}\right) C_{L_\delta}^\top \left(C_{L_\delta} C_{L_\delta}^\top\right)^{-1} - \delta\right] = 0 \tag{59}$$

Solving for δ gives the pseudo-inverse flap position vector δ_p

$$\delta_p = \frac{\left(C_L^* - C_{L_0} - \sum_{l=1}^{2} C_{L_{\alpha^l}} \alpha^{*l}\right) C_{L_\delta}^\top}{C_{L_\delta} C_{L_\delta}^\top} \tag{60}$$

The pseudo-inverse flap positions are the optimal flap positions that minimize the incremental lift coefficient which in turn also minimizes the incremental drag coefficient indirectly. This method does not require the estimation of the drag coefficient model parameters $C_{D_{\alpha^m}}$, $m = 1, \ldots, 6$, C_{D_δ}, and $C_{D_{\delta^2}}$ which could cause inaccuracy that would lead to incorrect optimal flap positions.

4. Analytical Optimization Method

The analytical optimization is developed to provide a quick one-pass solution without the need for iterating the solution. From the linear lift coefficient model in Eq. (5), the optimal angle of attack can be solved as

$$\alpha = \frac{C_L - C_{L_0} - C_{L_\delta}\delta}{C_{L_\alpha}} \tag{61}$$

Upon substitution α into the simplified quadratic drag coefficient model in Eq. (8), one gets

$$C_D = C_{D_0} + C_{D_\alpha}\left(\frac{C_L - C_{L_0} - C_{L_\delta}\delta}{C_{L_\alpha}}\right) + C_{D_\delta}\delta + C_{D_{\alpha^2}}\left(\frac{C_L - C_{L_0} - C_{L_\delta}\delta}{C_{L_\alpha}}\right)^2 + C_{D_{\delta^2}}\delta^2 \tag{62}$$

Taking the partial derivative of C_D with respect to δ yields

$$\left(\frac{\partial C_D}{\partial \delta}\right)^\top = C_{D_\delta}^\top - \frac{C_{D_\alpha} C_{L_\delta}^\top}{C_{L_\alpha}} - \frac{2C_{L_\delta}^\top C_{D_{\alpha^2}}\left(C_L - C_{L_0}\right)}{C_{L_\alpha}^2} + 2C_{D_{\delta^2}}\delta + \frac{2C_{L_\delta}^\top C_{D_{\alpha^2}} C_{L_\delta}\delta}{C_{L_\alpha}^2} \tag{63}$$

The optimal flap deflection δ^* is computed by setting $\left(\frac{\partial C_D}{\partial \delta}\right)^\top = 0$. This yields

$$\delta^* = \frac{C_{D_{\delta^2}}}{2}\left(I + \frac{C_{L_\delta}^\top C_{L_\delta}}{C_{L_\alpha}^2}\right)^{-1}\left[-C_{D_\delta}^\top + \frac{C_{D_\alpha} C_{L_\delta}^\top}{C_{L_\alpha}} + \frac{2C_{L_\delta}^\top C_{D_{\alpha^2}}\left(C_L^* - C_{L_0}\right)}{C_{L_\alpha}^2}\right] \tag{64}$$

where C_L^* is the target off-design lift coefficient.

The optimal angle of attack is evaluated as

$$\alpha^* = \frac{C_L^* - C_{L_0} - C_{L_\delta}\delta^*}{C_{L_\alpha}} \tag{65}$$

5. *Iterative Refinement Optimization Method*

The iterative refinement optimization method is designed to refine the optimal solution further to improve the accuracy of the real-time drag optimization algorithms after the first optimization cycle is completed. The objective of the iterative refinement cycle is to perturb the angle of attack about the approximately optimal angle of attack α^* and the flap position vector about the approximately optimal flap position vector δ^* both of which have been computed by the real-time drag optimization algorithm in order to locally improve the accuracy of the drag optimization. The perturbation lift coefficient and drag coefficient models can be formulated by neglecting all the higher order terms of the incremental angle of attack $\Delta\alpha$ in the nonlinear lift and drag coefficient models. This yields

$$\Delta C_L = C_L^* - C_L(\alpha^*, \delta^*) \approx \sum_{l=1}^{2} l C_{L_{\alpha^l}} \alpha^{*l-1} \Delta\alpha + C_{L_\delta} \Delta\delta \tag{66}$$

$$\Delta C_D = C_D^* - C_D(\alpha^*, \delta^*) \approx \sum_{m=1}^{6} m C_{D_{\alpha^m}} \alpha^{*m-1} \Delta\alpha + \frac{1}{2} \sum_{m=1}^{5} m(m-1) C_{D_{\alpha^m}} \alpha^{*m-2} \Delta\alpha^2 + \left(C_{D_\delta} + 2\delta^{*\top} C_{D_{\delta^2}}\right) \Delta\delta + \Delta\delta^\top C_{D_{\delta^2}} \Delta\delta \tag{67}$$

where $C_L(\alpha^*, \delta^*)$ and $C_D(\alpha^*, \delta^*)$ are the measured lift and drag coefficients at the approximately optimal angle of attack α^* and flap position vector δ^*.

If the measured lift coefficient is equal to the target off-design lift coefficient C_L^* to within a specified tolerance upon applying the perturbation input set of the commanded incremental angle of attack and flap positions, then the iterative refinement optimization is not necessary. Otherwise, the iterative refinement optimization computes the optimal incremental angle of attack $\Delta\alpha^*$ and flap position vector $\Delta\delta^*$ that further minimize the incremental drag coefficient ΔC_D while satisfying the incremental lift coefficient constraint. Solving for $\Delta\alpha$ from Eq. (66) gives

$$\Delta\alpha \approx \frac{\Delta C_L - C_{L_\delta} \Delta\delta}{\sum_{l=1}^{2} l C_{L_{\alpha^l}} \alpha^{*l-1}} \tag{68}$$

To minimize the incremental drag coefficient ΔC_D, the gradient of ΔC_D with respect to the incremental flap position vector $\Delta\delta$ is evaluated and then set to zero. This yields

$$\left(\frac{\partial \Delta C_D}{\partial \Delta\delta}\right)^\top \approx \sum_{m=1}^{6} m C_{D_{\alpha^m}} \alpha^{*m-1} \left(\frac{\partial \Delta\alpha}{\partial \Delta\delta}\right)^\top + \sum_{m=1}^{5} m(m-1) C_{D_{\alpha^m}} \alpha^{*m-2} \Delta\alpha \left(\frac{\partial \Delta\alpha}{\partial \Delta\delta}\right)^\top + \left(C_{D_\delta}^\top + 2C_{D_{\delta^2}} \delta^*\right) + 2C_{D_{\delta^2}} \Delta\delta = 0 \tag{69}$$

The optimal incremental flap position vector $\Delta\delta^*$ is then obtained as

$$\Delta\delta^* \approx \left[2C_{D_{\delta^2}} + \frac{C_{L_\delta}^\top C_{L_\delta} \frac{\partial^2 C_D^*}{\partial \alpha^2}}{\left(\frac{\partial C_L^*}{\partial \alpha}\right)^2}\right]^{-1} \left[-C_{D_\delta}^\top - 2C_{D_{\delta^2}} \delta^* + \frac{C_{L_\delta}^\top \left(\frac{\partial C_D^*}{\partial \alpha} \frac{\partial C_L^*}{\partial \alpha} + \Delta C_L \frac{\partial^2 C_D^*}{\partial \alpha^2}\right)}{\left(\frac{\partial C_L^*}{\partial \alpha}\right)^2}\right] \tag{70}$$

where the asterisk denotes the quantities evaluated at the approximately optimal angle of attack α^* and flap position vector δ^*.

6. *Optimization in the Presence of Non-Operative Flap Segments*

In order to anticipate a possible flap actuator failure which actually happened during the first test entry in September 2017, an adjustment to the optimization algorithms is made so that the actuator failure does not cause the real-time optimization algorithms to fail. In this case, some of the flap segments are assumed to fail in stuck positions, denoted by a flap position vector δ_{fail}. Let δ_{active} be the flap position vector for all the remaining functional flap segments such that $\delta_{active} \subset \delta$ and $\delta = \delta_{active} \cup \delta_{fail}$. Then, δ_{active} and δ_{fail} are mapped to δ as

$$\delta_{active} = G\delta \tag{71}$$

$$\delta_{fail} = H\delta \tag{72}$$

where $G \in \mathbb{R}^{n_{active} \times n_{flap}}$ and $H \in \mathbb{R}^{\left(n_{flap} - n_{active}\right) \times n_{flap}}$ with $n_{active} < n_{flap}$ being the number of the remaining functional flap segments.

Then, the lift coefficient and drag coefficient models are revised as

$$C_L = C_{L_{0,fail}} + \sum_{l=1}^{2} C_{L_{\alpha^l}} \alpha^l + C_{L_{\delta_{active}}} \delta_{active} \tag{73}$$

$$C_D = C_{D_{0_{fail}}} + \sum_{m=1}^{6} C_{D_{\alpha^m}} \alpha^m + C_{D_{\delta_{active}}} \delta_{active} + \delta_{active}^{\top} C_{D_{\delta^2_{active}}} \delta_{active} \tag{74}$$

where

$$C_{L_{0_{fail}}} = C_{L_0} + C_{L_\delta} H^{\top} \delta_{fail} \tag{75}$$

$$C_{L_{\delta_{active}}} = C_{L_\delta} G^{\top} \tag{76}$$

$$C_{D_{0_{fail}}} = C_{D_0} + \left(C_{D_\delta} + \delta_{fail}^{\top} H C_{D_{\delta^2}}\right) H^{\top} \delta_{fail} \tag{77}$$

$$C_{D_{\delta_{active}}} = \left(C_{D_\delta} + 2\delta_{fail}^{\top} H C_{D_{\delta^2}}\right) G^{\top} \tag{78}$$

$$C_{D_{\delta^2_{active}}} = G \hat{C}_{D_{\delta^2}} G^{\top} \tag{79}$$

Thus, the revised lift coefficient and drag coefficient models can then be identified and used in the real-time optimization drag algorithms without any further issues. The new model parameters $C_{L_{0_{fail}}}$, $C_{L_{\delta_{active}}}$, $C_{D_{0_{fail}}}$, $C_{D_{\delta_{active}}}$, and $C_{D_{\delta^2_{active}}}$ simply become the unknown model parameters to be estimated.

V. Wind Tunnel Experiment

Three wind tunnel test entries took place between September 2017 and June 2018. The results from these test entries are reported in the following subsections.

A. First Test Entry

The first test entry was conducted during the week of September 5, 2017. Originally, this test entry was the only planned test entry. Participated in the test were SSCI personnel, UW personnel, NASA personnel, and Boeing personnel as invited guests. Due to numerous hardware issues encountered, the wind tunnel test was aborted prematurely and the original test objectives were not achieved. The hardware issues were due to the complex nature of the actively controlled CRM wing with a large number of active control surfaces. This is perhaps the first ever attempt to design, build, and test such a complex actively controlled wind tunnel model with so many active control surfaces. So it is not entirely unexpected that hardware issues were encountered.

The primary cause is associated with the flap servos. The flap servo-actuator mechanisms are designed to fit in a tightly confined space to provide a clean aerodynamic surface with no external protuberances. The following observations are made:

- The flap servo-actuators presented the main operating challenge of the CRM wing during the first test entry. These Spektrum A7050 servos are small RC-type servos which were selected to allow them to fit compactly in the flap servo housing. Due to the confined space and lack of cooling, the servos would overheat. Another contributing factor is the direct drive design of the servos which caused the control hinge moment and aerodynamic loads to transfer directly to the servos. These contributing factors resulted in successive failures of the servos during the test.

- The encoders have no absolute position references. The flap servos have to be exercised through their full range of motion in order to find the encoder zero positions. The repetitive motion of the flap servos at their maximum limits caused further strain on the fragile servos during the test.

- The wiring for the servos is designed to be able to fit tightly in a confined space with limited physical access. Because the servos were frequently operating at close to their maximum load limits, the wiring was found to be inadequate for the amount of current that the servos required. During the last day of the test, the wiring suffered electrical shorts, resulting in the test aborted prematurely.
- The sidewall balance to which the wind tunnel model is mounted was found to have numerous issues such as not responding properly to the commands sent by the control system computer which communicates with the wind tunnel data acquisition system, and in some cases runaways.
- The wind tunnel model satisfies the design requirements for stiffness and wing tip deflection. The VCCTEF implementation satisfies the basic functionality for real-time drag optimization. The elastomer used to connect the flap segments by a bonding method to provide the continuous trailing edge was made of solid silicon rubber during the first test entry. These silicone rubber transition inserts were found to be quite stiff and thus exert additional resisting hinge moment loads on the flap servos which further exacerbated the servo problems. During the test, some of these silicone rubber transition inserts experienced cracking under high differential loads due to the relative flap positions.

During the test, data were acquired continuously by the wind tunnel data acquisition system and the control system developed by SSCI. The angle of attack signal from the sidewall balance was noticed to be too noisy to be used directly for the parameter estimation. The angle of attack signal was filtered by a time-averaged filter (over the last $3/4$ of a second) with outlier rejection to reduce noise to an acceptable level. Figure 17 shows the filtered angle of attack signal produced by the SSCI control system computer. Because of the filtering, the plan of acquiring data in a continuous mode for the recursive least-squares parameter estimation was not feasible. Instead, the data had to be acquired in a pitch-pause mode.

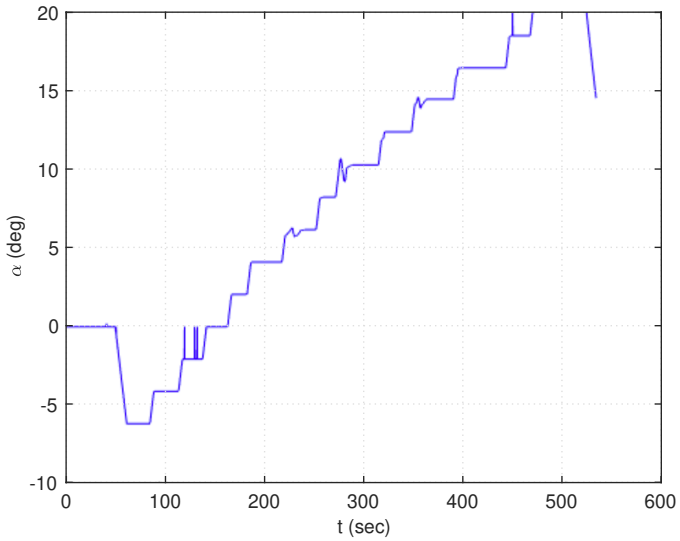

Figure 17. Filtered Raw Angle of Attack Acquired by SSCI Computer at $q_\infty = 10$ psf (September 2017)

The lift and drag measurements from the sidewall balance were also very noisy. Figures 18 and 19 show the unfiltered measured raw lift and drag signals produced by the control system computer. These raw force data are without the tare corrections which are normally applied to force measurements. As a result, the unfiltered drag force signal in Fig. 19 is noticed to be negative. The noise in the unfiltered lift force signal is noticed to drastically increase at about 260 sec which corresponds to an angle of attack of 6°. This increase in the noise level is most likely due to the increase in the unsteady lift force as the flow begins to separate. A first-order Butterworth filter was implemented to reduce the noise levels in the force signals to an acceptable level.

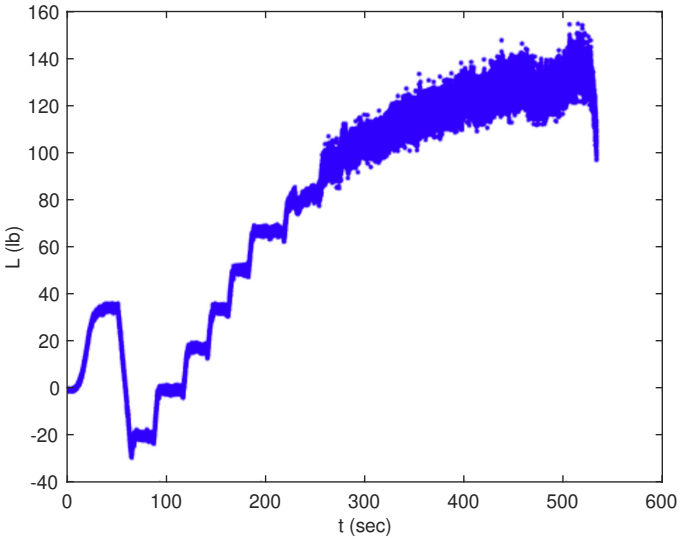

Figure 18. Unfiltered Raw Lift Force Acquired by SSCI Computer at $q_\infty = 10$ psf (September 2017)

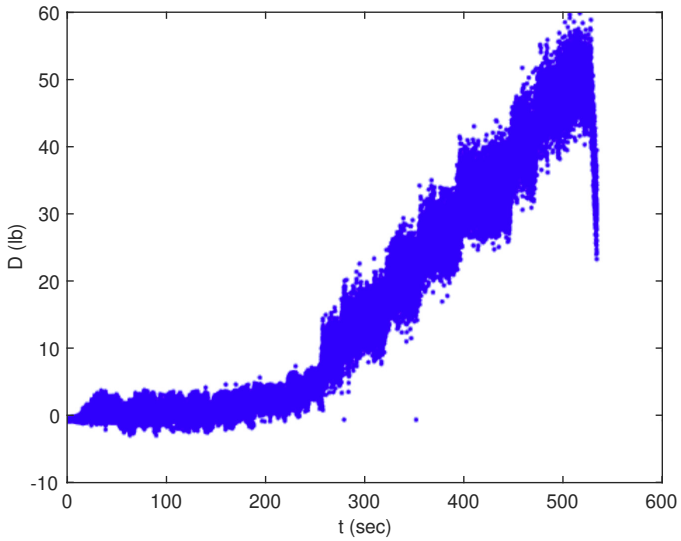

Figure 19. Unfiltered Raw Drag Force Acquired by SSCI Computer at $q_\infty = 10$ psf (September 2017)

A few data points were collected during one of the few angle-of-attack sweep runs at the dynamic pressure of 10 psf corresponding to a low subsonic speed of Mach 0.0822. The lift curve, drag polar, and the lift-to-drag ratio L/D plot of the clean wing configuration of the CRM wing are shown in Figs. 20, 21, and 22, respectively. The lift curve exhibits a considerable degree of nonlinearity at low angles of attack below 5° which could be due to the low Reynolds number at the test condition of 10 psf. The plan is to demonstrate the real-time drag optimization at a target off-design lift coefficient of $C_L^* = 0.65$ which represents a 30% increase in the design lift coefficient as the worst-case cruise lift coefficient. The angle of attack corresponding to the target off-design lift coefficient is estimated to be 7.3° which puts the lift curve of interest squarely in the nonlinear region. This observation motivates the use of the quadratic lift coefficient model in the real-time drag optimization strategy.

The lift curve slope C_{L_α} at low angles of attack below 5° is estimated to be 3.4543. The theoretical C_{L_α} for a rigid

wing can be estimated to be 4.4144 using the formula

$$C_{L_\alpha} = \frac{2\pi \cos \Lambda_{c/2}}{\sqrt{1 - M_\infty^2 \cos^2 \Lambda_{c/2}} + \frac{2 \cos \Lambda_{c/2}}{A.R.\varepsilon}} \tag{80}$$

where $\Lambda_{c/2}$ is the mid-chord sweep angle which is estimated to be about 30°, $A.R.$ is the aspect ratio, and ε is the span efficiency factor which is assumed to be 0.9.

The L/D ratio of the CRM wing attains a maximum value of 23.33 at $C_L = 0.3566$. The L/D ratio at the design $C_L = 0.5$ is about 22.07 which is almost at the maximum value. This suggests that the CRM wing is nearly optimal with the new jig-shape twist.

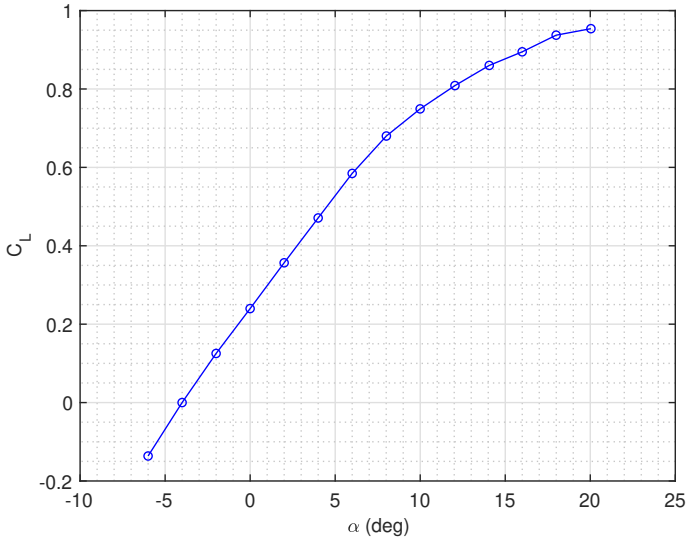

Figure 20. Lift Coefficient vs. Angle of Attack of Clean Wing at $q_\infty = 10$ psf (September 2017)

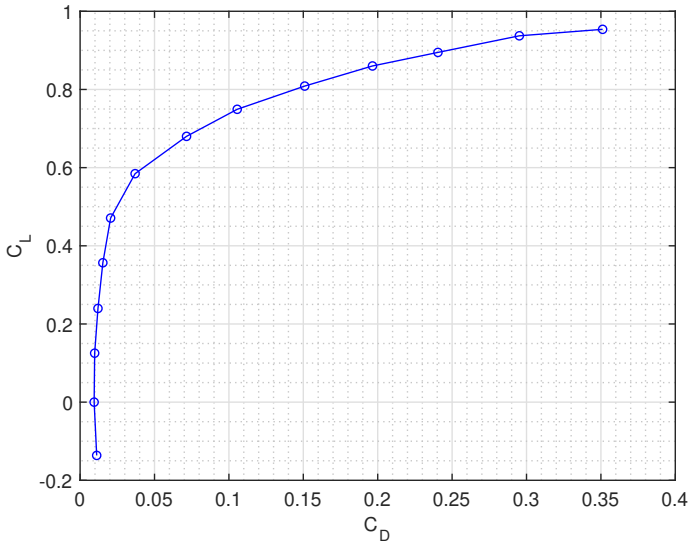

Figure 21. Drag Polar of Clean Wing at $q_\infty = 10$ psf (September 2017)

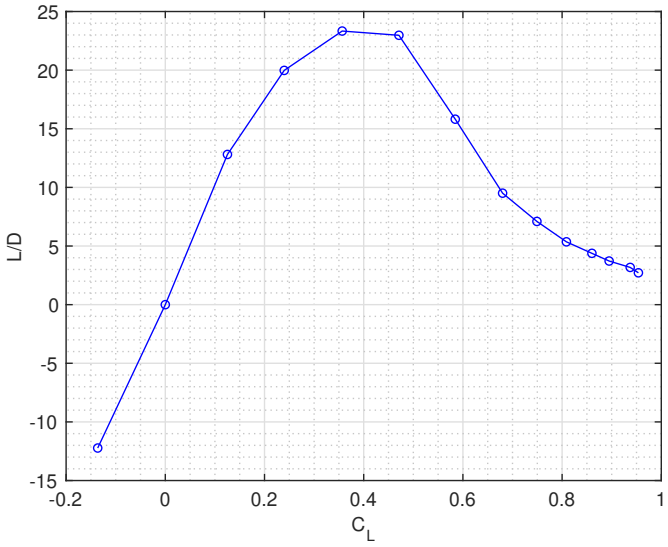

Figure 22. L/D Curve of Clean Wing at $q_\infty = 10$ psf (September 2017)

The VICON system also acquired the wing vertical displacement under the aerodynamic loading during the test. Figures 23 and 24 show the vertical displacements measured by the VICON system at the wing tip leading edge location L14 and the trailing edge location T14 (see Fig. 13). The wing tip vertical bending displacement can be computed as the average of the two vertical displacements which gives a value of 8.5 inches. This vertical bending displacement turns out to be precisely 10% of the wing semi-span as designed. The vertical displacement data also suggests a nose-down torsional twist. The vertical displacement differential between the leading edge and trailing edge is about -0.58 inches. If the distance between the locations L14 and T14 is about equal to the tip chord of 8.8 inches, then the wing tip torsional twist is about -3.8°.

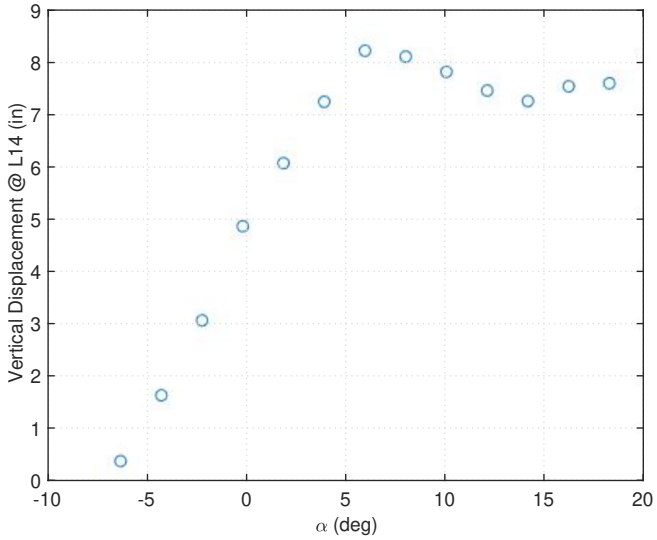

Figure 23. Vertical Displacement at Location L14 at $q_\infty = 10$ psf (September 2017)

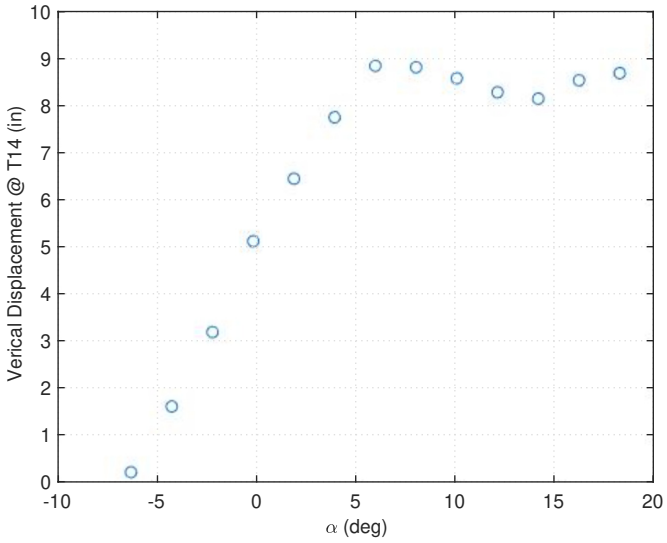

Figure 24. Vertical Displacement at Location T14 at $q_\infty = 10$ psf (September 2017)

B. Second Test Entry

During the following months after the first test entry, the hardware issues were actively addressed by a complete redesign of the servo hardware and wiring. Another attempt to re-start the wind tunnel test was made during the week of December 4, 2017, but the wing was still not ready. A second test entry was scheduled during the week of April 9, 2018. During this test entry, an issue was encountered with the sidewall balance drive motor which communicates the angle of attack to the control system computer. This issue and the model calibration took almost the whole entire week. The test finally began on April 13 and ended on April 19. A total of 89 runs were acquired during this test entry. Because of the previous issue encountered with the sillicone rubber transition inserts, these inserts were removed from the wing for the initial portion of the test while the 3D-printed transition inserts were still in fabrication. The flap system thus is referred to as a variable camber discrete trailing edge flap (VCDTEF). The 3D-printed transition inserts were installed on the wing starting with run 72 on April 19.

Both NASA Newton-Raphson optimization algorithm and SSCI genetic algorithm were exercised during the test. However, they both produced unexpected results which did not produce the expected drag reduction. A preliminary investigation revealed that the onboard aerodynamic model identification RLS algorithm was not able to accurately estimate the model parameters perhaps due to insufficient and or noisy data, uncertainty in the flap positions, and the general experimental uncertainty.

Figure 25 shows the range of the flap positions of the VCDTEF configured in a circular arc camber during an optimization run on April 18 at 14:48 hour PDT. Flap 1B position varies as much as -1.2°. Flap 3A was apparently inoperative during this run as well as during the entire test. It should be noted that the flap positions have an uncertainty of about 1 degree. So the exact flap positions could be quite different from the values indicated in Fig. 25.

Figures 26-31 show the parameter estimates computed by the RLS algorithm. These figures reveal the problem with the onboard aerodynamic model identification RLS algorithm. The same set of data was analyzed during the post-test analysis using the BLS algorithm. The test was conducted at $q_\infty = 10$ psf which is used throughout the test unless otherwise noted. All the 6 elements of the cross term drag sensitivity vector $C_{D_{\alpha\delta}}$ and the 18 elements of the quadratic drag sensitivity matrix $C_{D_{\delta^2}}$ were estimated.

Figure 26 shows the estimates of C_{L_0}, C_{L_α}, and $C_{L_{\alpha^2}}$. The C_{L_0} estimate computed by RLS algorithm converges to a large value. Its estimate computed by BLS algorithm is smaller and agrees with the lift coefficient data as shown in Fig. 32. Comparing this lift curve to the lift curve from the first test entry, it is apparent that they are not the same. The change in C_{L_0} is unexplained. One possible explanation is that the reference zero angle of attack in the sidewall balance could somehow be set differently from that in the first test entry. Another possible explanation is that Flap 3A could have failed in a stuck positive downward position which would have cause the lift coefficient to increase. The lift curve in the second test entry is also more linear than that in the first test entry. This is likely due to the use of the boundary layer transition trip strip on the wing at the leading edge in the second test entry. The C_{L_α} estimate

computed by the RLS algorithm converges to a negative value which is troubling whereas its estimate computed by the RLS algorithm is positive and is correct.

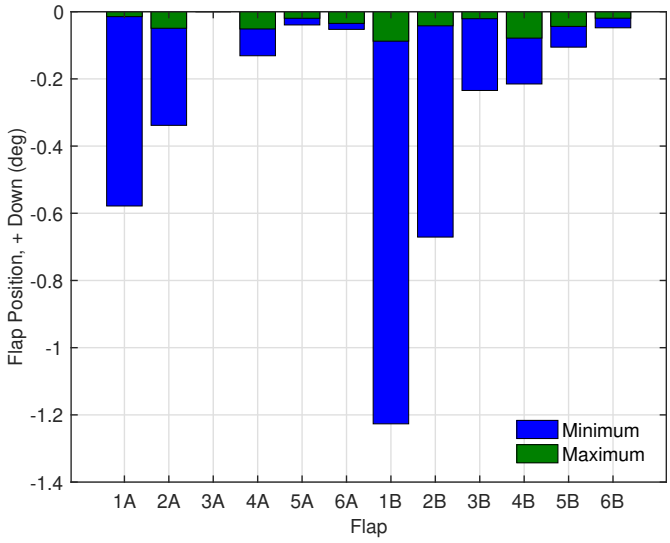

Figure 25. Flap Position Range (April 18, 2018 @ 14:48 PDT)

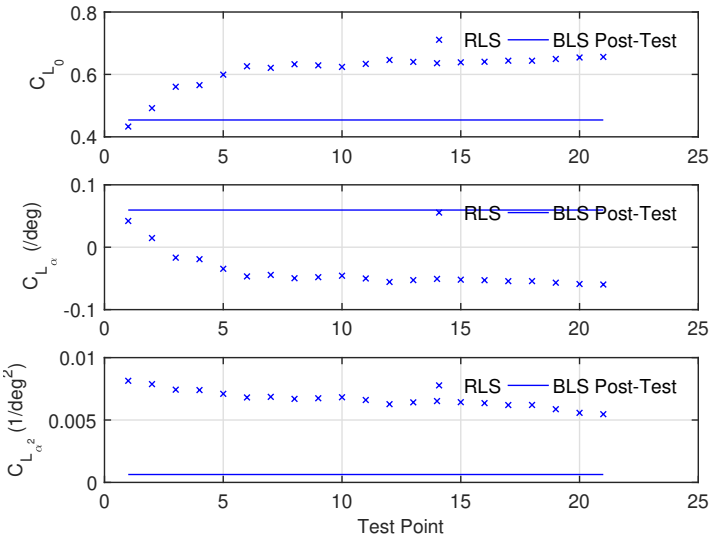

Figure 26. C_{L_0}, C_{L_α}, and $C_{L_{\alpha^2}}$ Estimated by RLS and BLS (April 18, 2018 @ 14:48 PDT)

Figure 27 shows the estimates of C_{D_0}, C_{D_α}, and $C_{D_{\alpha^2}}$. The C_{D_0} estimate computed by the RLS algorithm converges to a similar value computed by the BLS algorithm. The most troubling result is the negative value of the $C_{D_{\alpha^2}}$ estimate computed by the RLS algorithm. This quantity is a dominating drag coefficient parameter which should be positive. The sign error suggests a serious issue with the RLS algorithm.

Figures 28 and 29 show the estimates of C_{L_δ}. All but one of the C_{L_δ} estimates computed by the RLS algorithm converge to negative values. In theory, the values of C_{L_δ} should be positive. The sign reversal could indicate the potential issue with the uncertainty in the flap positions due to the mechanical backlash and the encoder resolution. There is a significant discrepancy between the RLS estimates and the BLS estimates.

Figures 30 and 31 show the estimates of C_{D_δ}. Almost all of the C_{D_δ} estimates computed by the RLS algorithm

converge to very small values near zero.

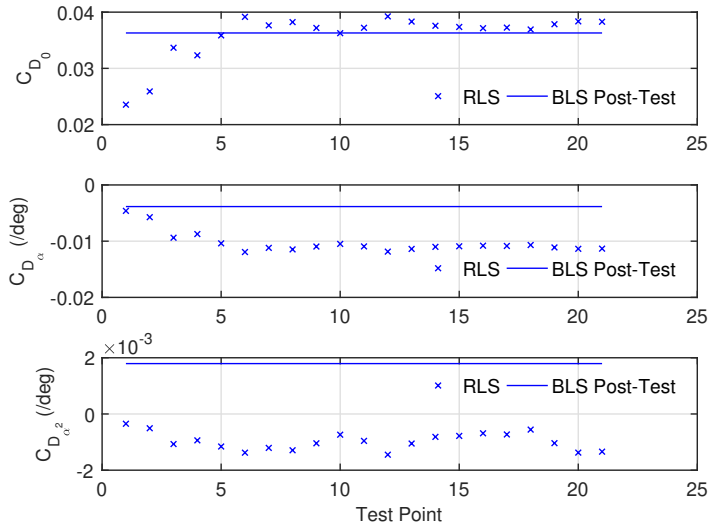

Figure 27. C_{D_0}, C_{D_α}, **and** $C_{D_{\alpha^2}}$ **Estimated by RLS and BLS (April 18, 2018 @ 14:48 PDT)**

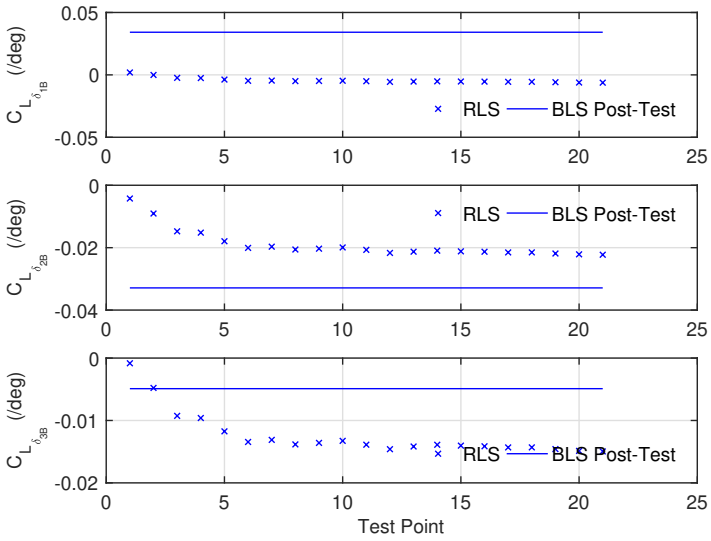

Figure 28. $C_{L_{\delta_{1B}}}$, $C_{L_{\delta_{2B}}}$, **and** $C_{D_{\delta_{3B}}}$ **Estimated by RLS and BLS (April 18, 2018 @ 14:48 PDT)**

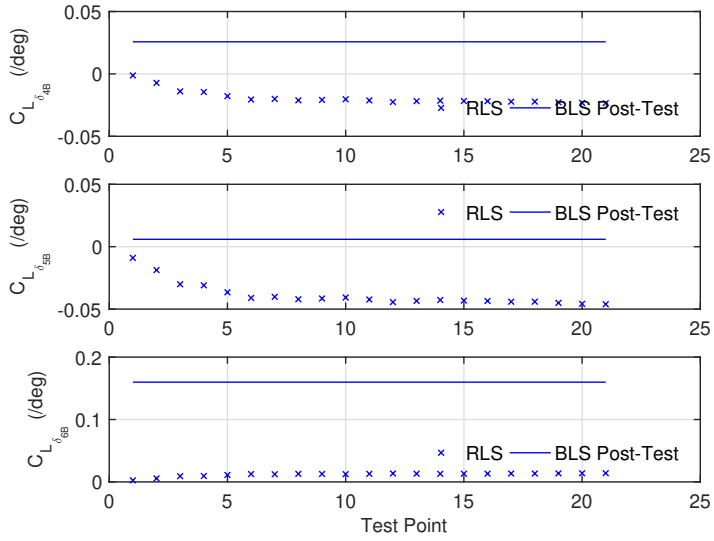

Figure 29. $C_{L_{\delta_{4B}}}$, $C_{L_{\delta_{5B}}}$, **and** $C_{D_{\delta_{6B}}}$ **Estimated by RLS and BLS (April 18, 2018 @ 14:48 PDT)**

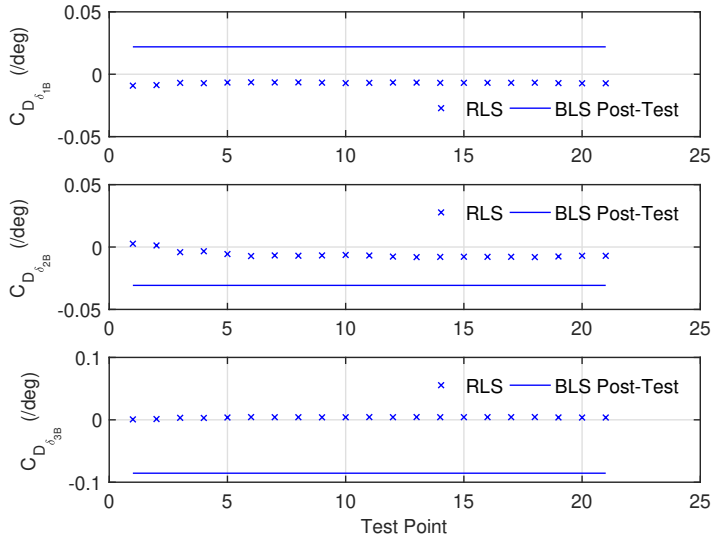

Figure 30. $C_{L_{\delta_{4B}}}$, $C_{L_{\delta_{5B}}}$, **and** $C_{D_{\delta_{6B}}}$ **Estimated by RLS and BLS (April 18, 2018 @ 14:48 PDT)**

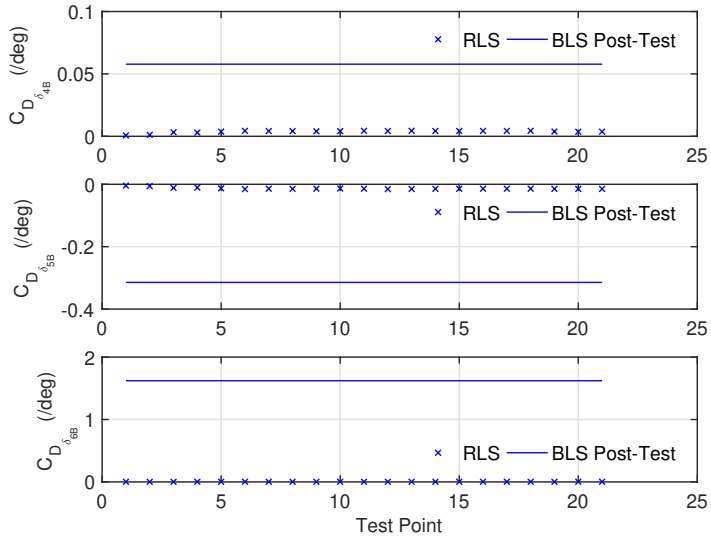

Figure 31. $C_{L_{\delta_{4B}}}$, $C_{L_{\delta_{5B}}}$, **and** $C_{D_{\delta_{6B}}}$ **Estimated by RLS and BLS (April 18, 2018 @ 14:48 PDT)**

Figure 32 is the plot of lift curves of the clean wing for three different runs over a range of the angle of attack from -15° to 13°. The lift coefficient data from these three runs which were taken over three different days from April 17 to April 19 show very good repeatability. The lift curve slope C_{L_α} in the linear region is estimated to be 3.7216. Figure 33 is the plot of the drag polars for the three runs. The drag coefficient data show very good repeatability. The low drag region appears to correspond to a range of the lift coefficient between -0.45 and 0.7. Figure 34 is the plot of the L/D ratios for the three runs, showing a maximum L/D ratio of about 25.35 at $C_L = 0.6$. Comparing to the maximum L/D ratio of 23.33 at $C_L = 0.3566$ in the first test entry, the wing in the second test entry is aerodynamically different from the wing in the first test entry.

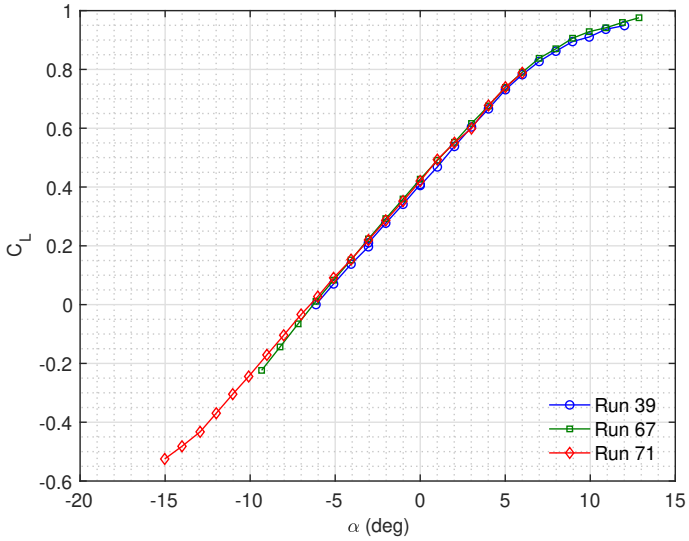

Figure 32. Lift Curves of Clean Wing (April 2018)

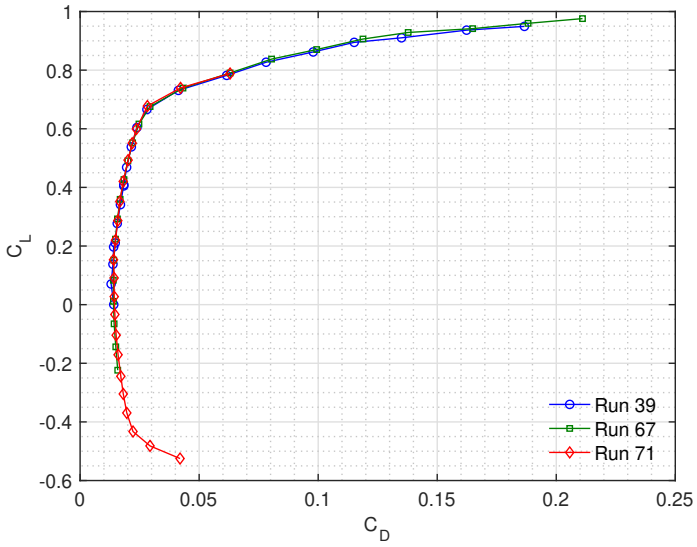

Figure 33. Drag Polars of Clean Wing (April 2018)

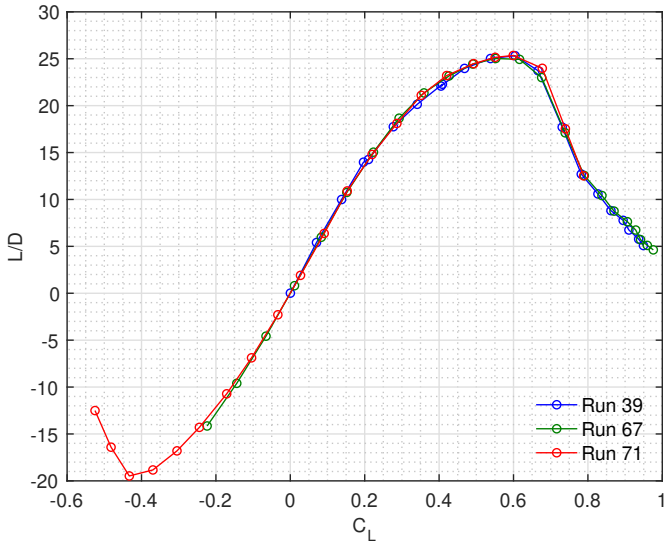

Figure 34. L/D Curves of Clean Wing (April 2018)

Figure 35 is the plot of the lift curves for run 71 with the VCDTEF and run 72 with the VCCTEF when the 3D-printed transition inserts were first installed on the wing. Prior to run 72, the gaps between the flap segments were not covered. Spacers were made to bring the flap side edges closer to each other to within a measured tolerance of $1/16$ inches. This tight gap is as close as it can be made without causing rubbing. This flap configuration is referred to as VCDTEF. Figure 35 perhaps presents for the first time the effect of the continuous trailing edge on the lift coefficient which can be seen to be quite significant. The VCCTEF produces an incremental lift coefficient ΔC_L of 0.0386 at the zero angle of attack or equivalently a reduction in the angle of attack of 0.48°. The lift reduction associated with the VCDTEF is due to the flow leakage through the small flap gaps which causes spanwise vortices to form. The spanwise vortices effectively cause the lift distribution to reduce toward the flap side edges.

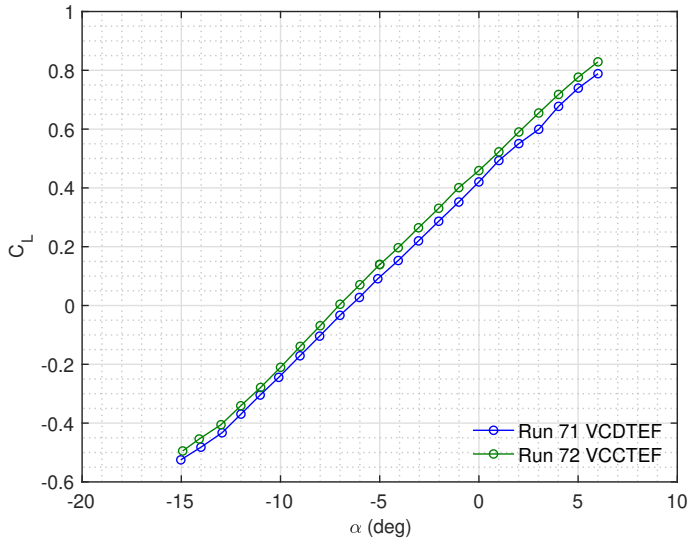

Figure 35. Lift Curves of Clean Wing with VCDTEF and VCCTEF (April 2018)

Figure 36 presents for the first time the effect of the continuous trailing edge on the drag coefficient which is significant in the operating range of the lift coefficient between 0.35 and 0.65 ($\pm 30\%$ over the design lift coefficient $C_L = 0.5$). The difference in the drag coefficient is 13 counts (1 drag count = 0.0001) or 5% at $C_L = 0.65$ and 2 counts or 1.4% at $C_L = 0.35$. It is of an academic interest to note that at negative lift the VCCTEF actually produces more drag than the VCDTEF.

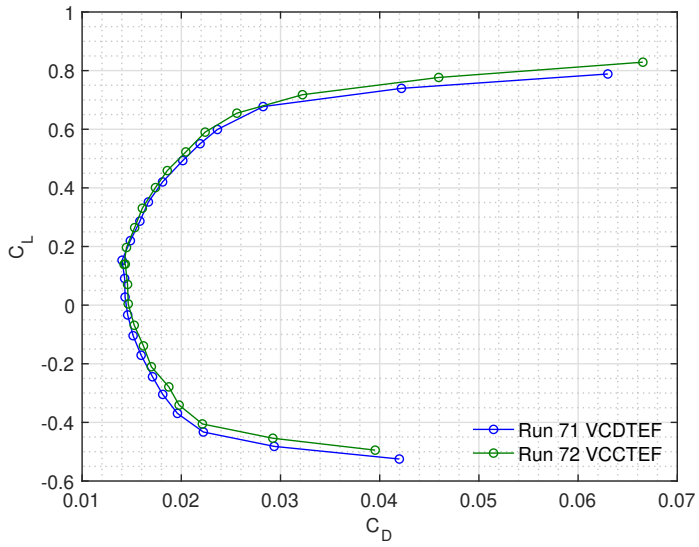

Figure 36. Drag Polars of Clean Wing with VCDTEF and VCCTEF (April 18, 2018 @ 14:48 PDT)

Figure 37 is the plot of the L/D ratios for the VCDTEF and VCCTEF. The VCCTEF produces a L/D ratio of 26.34 which is a 4% increase from the L/D ratio of 25.35 for the VCDTEF.

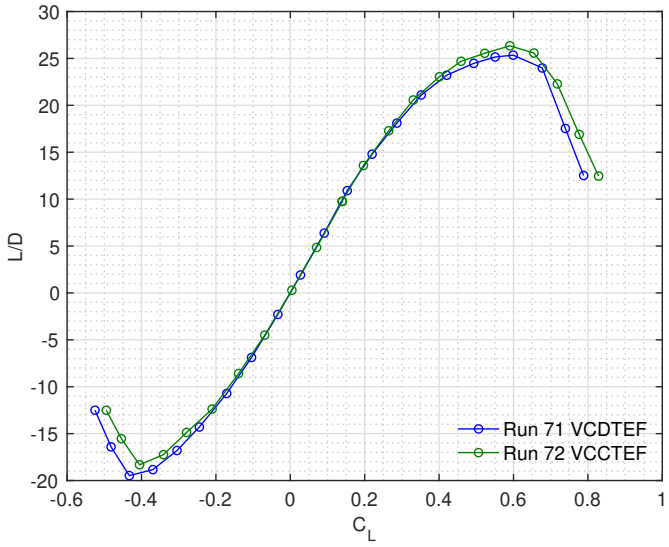

Figure 37. L/D Curves of Clean Wing with VCDTEF and VCCTEF (April 2018)

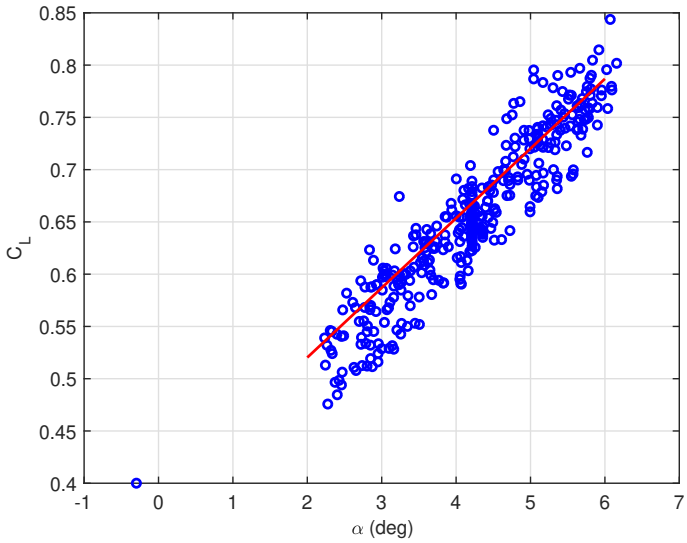

Figure 38. Regression Analysis of Lift Coefficient

Because of the issue with the onboard aerodynamic model identification, both SSCI and NASA real-time drag optimization algorithms failed to produce meaningful solutions. SSCI conducted a post-test optimization but all the optimization runs resulted in predicting a negative drag coefficient. NASA also conducted a post-test optimization but the results are more encouraging. A regression analysis was performed on the recorded test data from 13 runs from April 13 to April 18 as shown in Figs. 38 and 39 which show the lift and drag coefficients as functions of the angle of attack. The lift and drag coefficients are then constructed from the regression for the post-test drag optimization for a target design $C_L^* = 0.65$. The post-test optimization produces the optimal flap positions as shown in Fig. 40 corresponding to an angle of attack of 3.61°. A circular arc camber is used and flap 3A is set to zero. The regression analysis produces a clean wing drag coefficient of 325 counts as compared to 270 counts from the clean wing test data. The optimization produces a drag coefficient of 258 counts which represents a drag reduction of 67 counts or 20%. For the obvious reason, this drag reduction is overly optimistic since the regression over-predicts the drag coefficient. Nonetheless, the post-test optimization results suggest that the real-time drag optimization could achieve a significant

drag reduction at the target off-design $C_L^* = 0.65$. This gives the confidence that an optimal solution could be found during the next test entry provided that no further setback would be encountered.

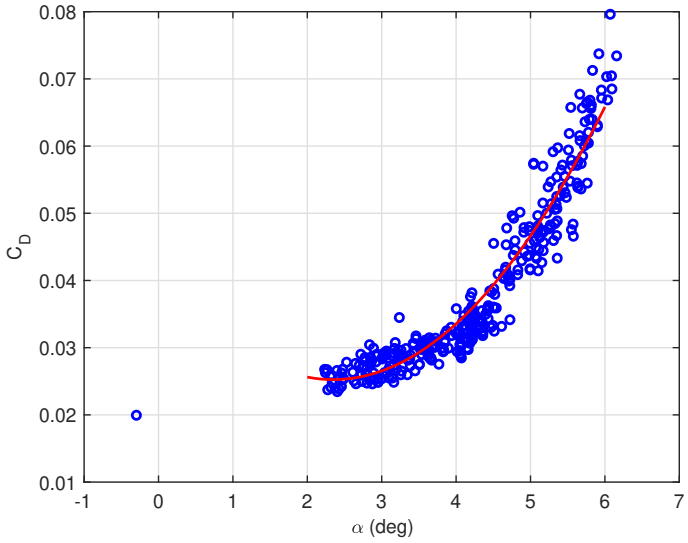

Figure 39. Regression Analysis of Drag Coefficient

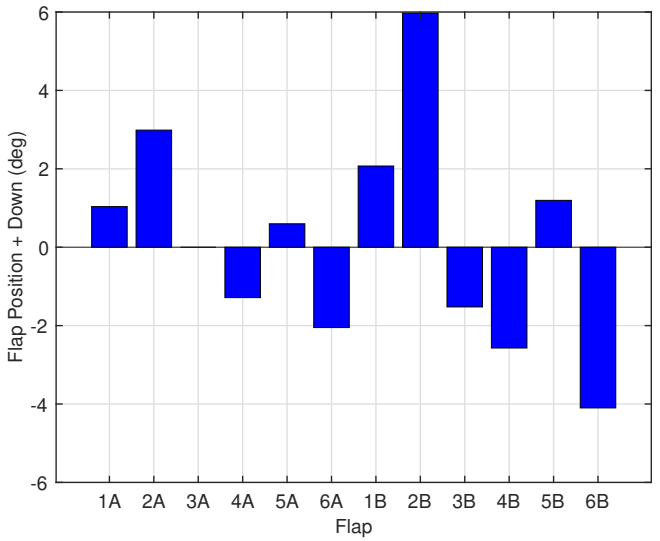

Figure 40. Flap Positions Computed Off-Line Optimization

The SBIR Phase II contract with SSCI concluded with the second test entry. NASA decided to further pursue the additional testing. A plan was developed following the second test entry to resolve the issues encountered with the RLS algorithm. This plan includes adding the BLS algorithm, which is shown in simulations to work better than RLS method, and also the iterative angle-of-attack seeking method in order to speed up the test, as well as a number of additional real-time drag optimization algorithms.

C. Final Test Entry

The third and final test entry took place during the week of June 25, 2018 and concluded on July 2, 2018. The test was conducted by NASA personnel as SSCI completed their contract requirements with the second test entry in spite

of not being able to fully meet the test objectives.

A root-cause analysis was conducted over the month of April and May, leading to the conclusion that the issues with the RLS algorithm could be traced to the initialization of the algorithm. It appears that the initial values of the covariance matrix and the parameter estimates were not properly set, thereby causing the onboard aerodynamic model identification to fail to converge to the correct values. Several changes and improvements are made to the RLS and real-time drag optimization algorithms as follows:

1. The initialization of the RLS algorithm are updated with better initial values.
2. Nonlinear lift and drag coefficient models are added as the data from the second test entry suggest.
3. The BLS algorithm is added since it is seen to perform better than the RLS algorithm. The BLS algorithm processes the data all at once when enough data are acquired as opposed to the RLS algorithm which processes the data as they stream in one at a time.
4. The iterative gradient optimization method is developed to improve upon the second-order Newton-Raphson optimization method.
5. The pseudo-inverse optimization method is also developed to offer an alternative real-time drag optimization method that does not required a drag coefficient model which greatly simplifies the real-time drag optimization strategy.
6. The iterative angle-of-attack seeking method is developed to speed up the test since the current random excitation method is rather slow and can take a long time to acquire enough data for onboard aerodynamic model identification.
7. General software fixes are also made to fix minor issues with the software.

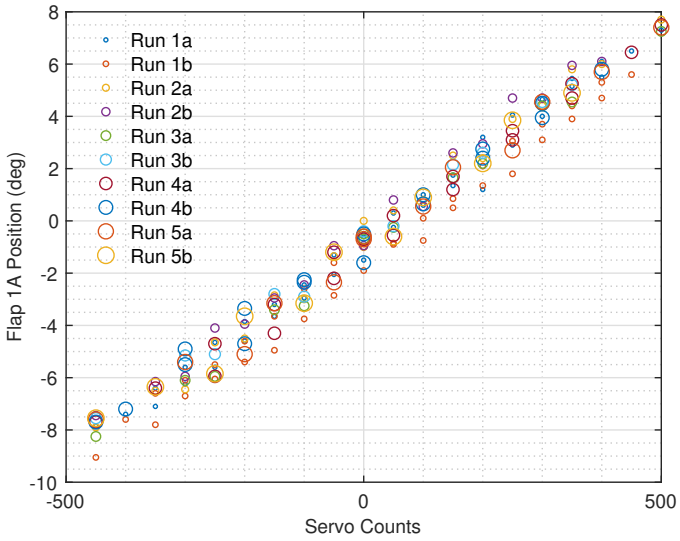

Figure 41. Flap 1A Calibration (May 2018)

Because of the low accuracy in the flap positions observed during the second test entry, a detail investigation of the flap position uncertainty was conducted prior to the third test entry. A calibration was carried out in between the second and third test entries to compare the flap positions against the servo counts. Figure 41 shows the calibration data collected for Flap 1A. A least-squares regression is performed and the error distribution is computed to determine the flap position errors for the individual flap segments. Figure 42 shows the error distribution of Flap 1A. The largest error distribution of Flap 1A occurs at an average flap position error of -0.121°. The range of the flap position error for Flap 1A is between -0.995° and 1.12°. Figure 43 shows the average flap position error distribution for all the flap segments computed from the calibration data. Flap 2B has the largest average flap position error of -0.358°. Figure 44 shows the standard deviation in the flap position error for all the flap segments. Flap 5B has the largest standard

deviation of 1.0318° in the flap position error. This flap proves to be troublesome for the real-time drag optimization algorithms. The mean standard deviation is 0.3846°. The flap uncertainty analysis shows that on an average the flap position errors could be about ±0.4° with some flap segments experiencing more or less than this amount.

The third test entry is generally a successful test. It was able to demonstrate successfully the real-time drag optimization strategy for the first time since the test started in September 2017. The third test entry also identifies some lingering issues with the flap actuators. There is a large discrepancy between the commanded flap positions and the actual measured flap positions using an inclinometer, thereby occasionally requiring manual verification of the flap positions in between some optimization runs. The servos experienced a runaway problem during the test, thereby causing overstressing and damage to the flap servos and the 3D-printed transition inserts.

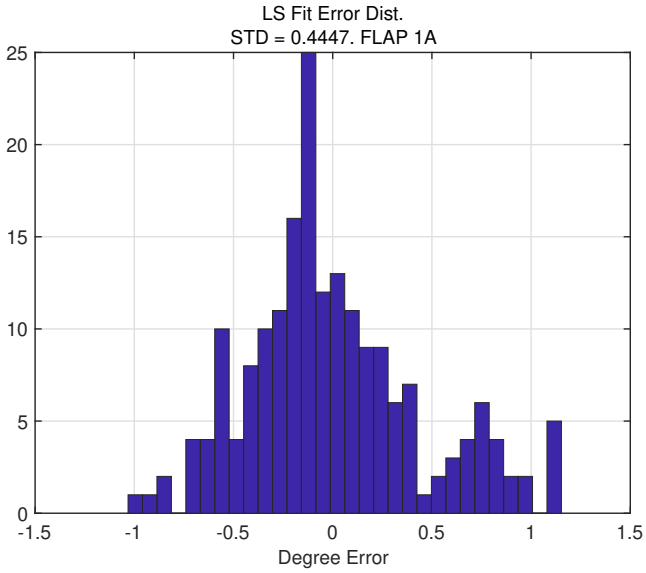

Figure 42. Flap 1A Error Distribution (May 2018)

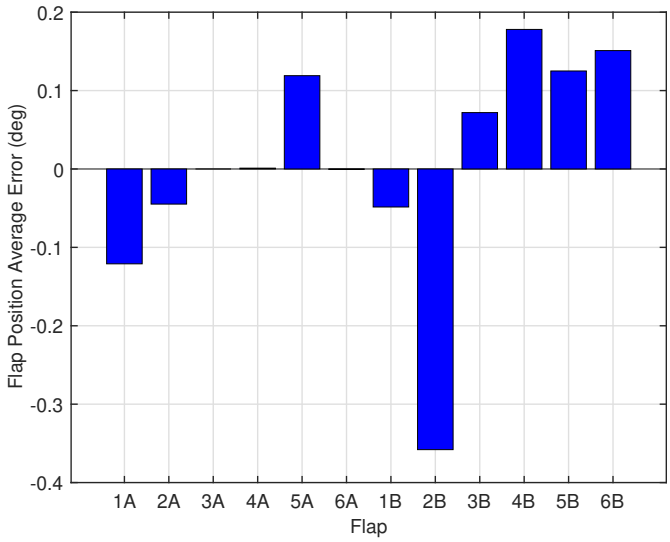

Figure 43. Flap Average Position Errors (May 2018)

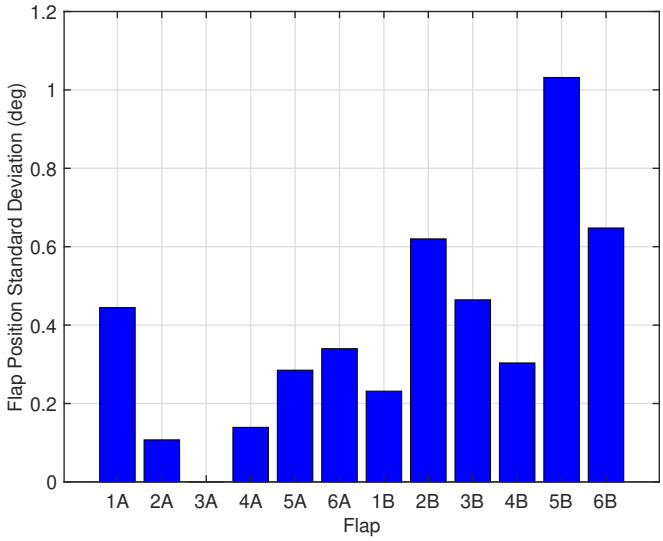

Figure 44. Flap Position Standard Deviations (May 2018)

Two target off-design lift coefficients were selected: C_L^* =0.65 and $C_L^* = 0.7$. The off-design $C_L^* = 0.65$ represents a 30% increase over the design $C_L = 0.5$ as suggested by Boeing. The off-design $C_L^* = 0.7$ is selected to provide more sensitivity to the real-time drag optimization since the maximum L/D ratio occurs near the off-design $C_L^* = 0.65$. During the initial part of the test, the onboard aerodynamic model identification uses the RLS algorithm to perform the parameter estimation. The linear lift coefficient model and simplified quadratic drag coefficient model are used. The analytical optimization method is used to compute the optimal angle of attack and flap positions. During the latter part of the test, the iterative angle-of-attack seeking method is used to identify the onboard aerodynamic model using the BLS algorithm. The nonlinear lift and drag coefficient models are used during this portion of the test. Both the iterative gradient optimization method and the pseudo-inverse optimization method are used to compute several optimal solutions. During this portion of the test, the servos became problematic, thus resulting in the manual setting of the flap positions.

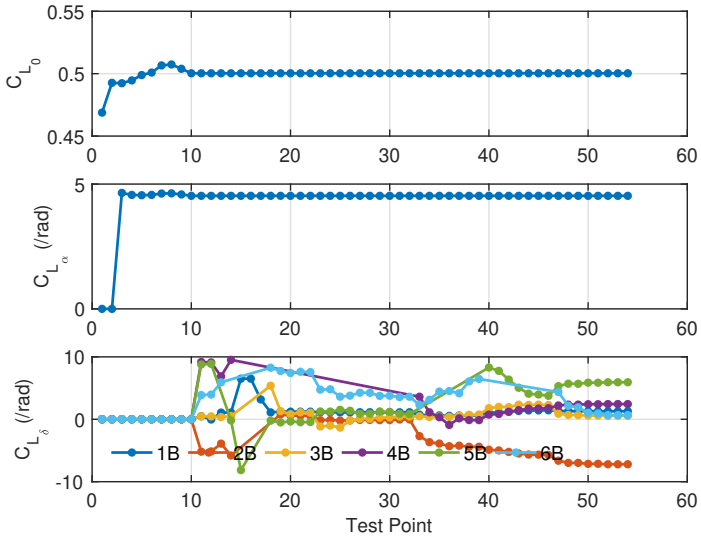

Figure 45. C_{L_0}, C_{L_α}, and C_{L_δ} Estimated by RLS for Run 19 (June 2018)

Figure 45 shows the estimates of C_{L_0}, C_{L_α}, and C_{L_δ} computed by the RLS algorithm for Run 19. The parameter

convergence of C_{L_0} and C_{L_α} is achieved quickly after no more than 10 test points. These parameter estimates converge to their approximately correct values which are positive as expected. The C_{L_δ} estimates converge much more slowly than the C_{L_0} and C_{L_α} estimates. The C_{L_δ} estimates for all the flap segments except Flap 2B converge to positive values as expected.

Figure 46 shows the estimates of C_{D_0}, C_{D_α}, and $C_{D_{\alpha^2}}$ computed by the RLS algorithm for Run 19. All of these parameter estimates converge to positive values as expected. The parameter convergence is achieved quickly after no more than 10 test points.

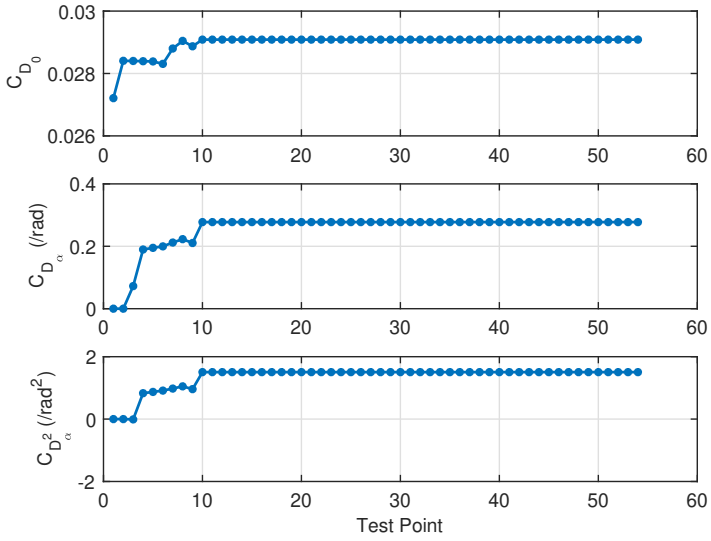

Figure 46. C_{D_0}, C_{D_α}, and $C_{D_{\alpha^2}}$ Estimated by RLS for Run 19 (June 2018)

Figure 47 shows the estimates of C_{D_δ} and $C_{D_{\delta^2}}$ computed by the RLS algorithm for Run 19. These parameter estimates converge much more slowly than the C_{D_0}, C_{D_α}, and $C_{D_{\alpha^2}}$ estimates. The C_{D_δ} estimates for all the flap segments except Flap 2B converge to positive values as expected. The $C_{D_{\delta^2}}$ estimates for all the flap segments except Flap 5B also converge to positive values as required.

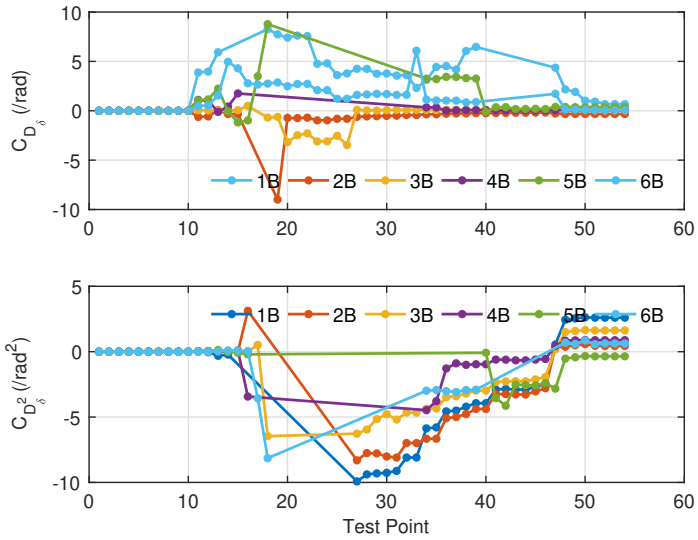

Figure 47. C_{D_δ} and $C_{D_{\delta^2}}$ Estimated by RLS for Run 19 (June 2018)

Using the converged parameter estimates computed by the RLS algorithm, the analytical optimization is used to compute the optimal angle of attack to be 1.41° and the flap positions as shown in Fig. 48. Flap 1B is seen to be the most dominant in the optimal solution. Flaps 4B, 5B, and 6B are rather inactive.

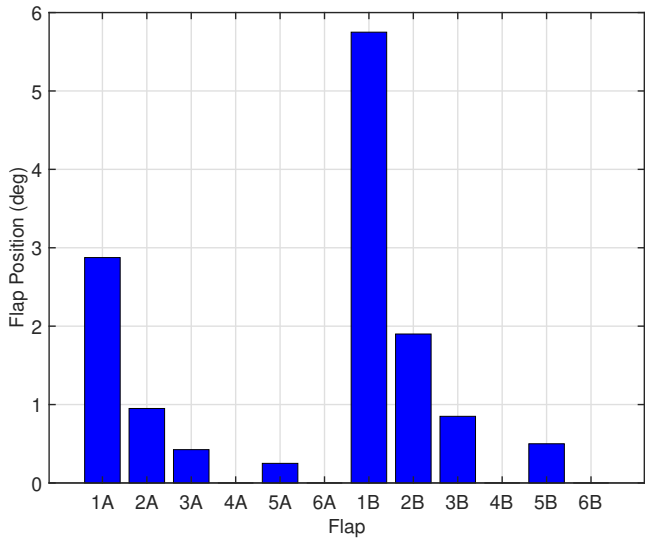

Figure 48. Flap Positions Computed by Analytical Optimization for Run 24 (June 2018)

Figure 49 shows the lift curve for the analytical optimization Run 24 as compared to the lift curves for the clean wing Runs 2, 10, and 22. With the flap segments deployed in their computed flap positions, the lift curve shifts to the left, resulting in a reduction in the angle of attack at the same off-design $C_L^* = 0.65$.

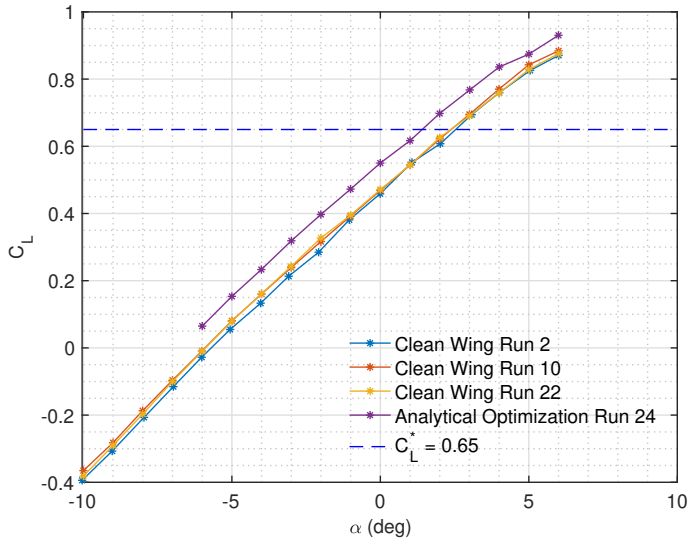

Figure 49. Lift Curve Comparison of Analytical Drag Optimization (June 2018)

Figure 50 shows the drag polar for the analytical optimization Run 24 in comparison to the drag polars for the clean wing. The drag coefficient for Run 24 is 324 counts. The average drag coefficient for the clean wing is 332 counts. Therefore, an 8 count or 2.4% drag reduction is achieved by the analytical optimization method. This drag optimization run demonstrates successfully the real-time drag optimization objective of the wind tunnel test. The drag reduction at the off-design $C_L^* = 0.65$ is small relative to the post-test optimization results.

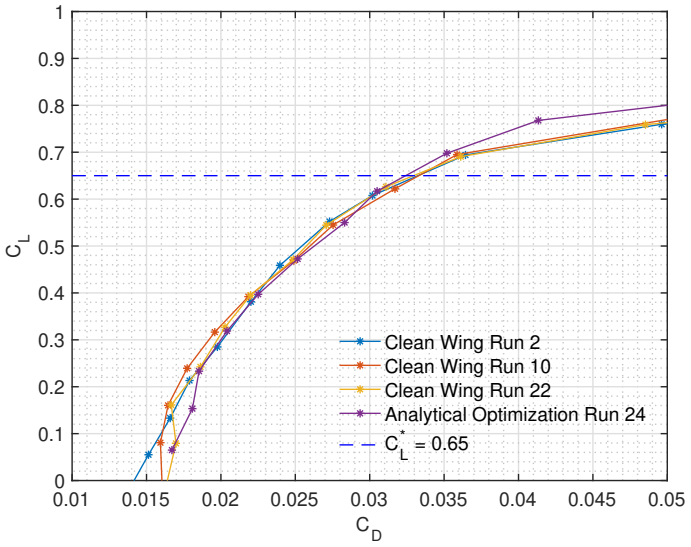

Figure 50. Drag Polar Comparison of Analytical Drag Optimization (June 2018)

Figure 51 shows the L/D ratio for the analytical optimization Run 24 as compared to the L/D ratios for the clean wing Runs 2, 10, and 22. It is interesting to note that the maximum L/D ratio for the analytical optimization Run 24 is about the same as the maximum L/D ratios for the clean wing but occurs at a different lift coefficient. The real-time drag optimization causes the L/D curve to shift to the right. This causes the L/D ratio to increase over that of the clean wing at the off-design $C_L^* = 0.65$. It also should be noted that the maximum L/D ratio for the CRM wing in the third test entry is smaller than that for the CRM wing in the second test entry. Thus, the two wings are aerodynamically different.

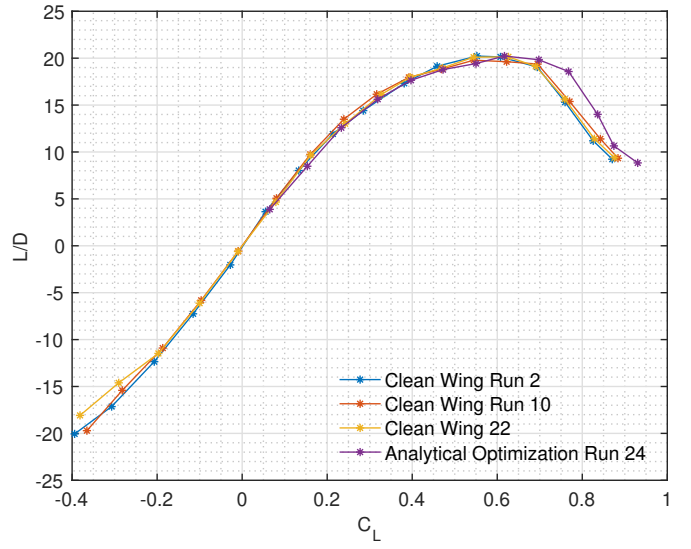

Figure 51. L/D Curve Comparison of Analytical Drag Optimization (June 2018)

At this point in the test, the nonlinear lift and drag coefficient models are used as test data from Run 25 suggest. Figure 52 illustrates the lift curve for the clean wing Run 25. As seen, there is a nonlinear behavior in the lift curve. The linear lift coefficient model does not correlate well with the lift curve data. The quadratic lift coefficient model achieves a much better correlation than the linear lift coefficient model.

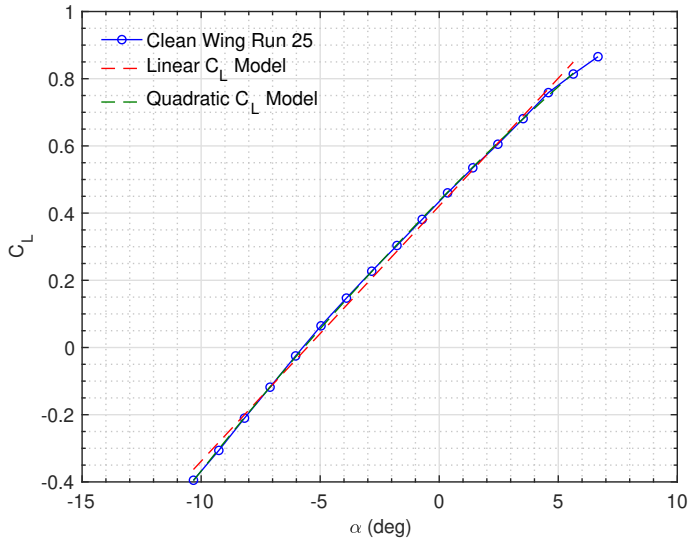

Figure 52. Lift Coefficient Correlation for Run 25 (June 2018)

Figure 53 illustrates the drag curve C_D vs. α for the clean wing Run 25. Both the quadratic and quartic drag coefficient models correlate well the drag curve data between the angles of attack of -5° and 3.5°. At the angle of attack of 3.5°, the drag coefficient abruptly increases and no longer follows the quadratic and quartic drag coefficient models, thereby suggesting that the wing perhaps starts encountering stall at this angle of attack. The 6^{th}-order drag coefficient model, on the other hand, correlates well up to an angle of attack of 5.5°.

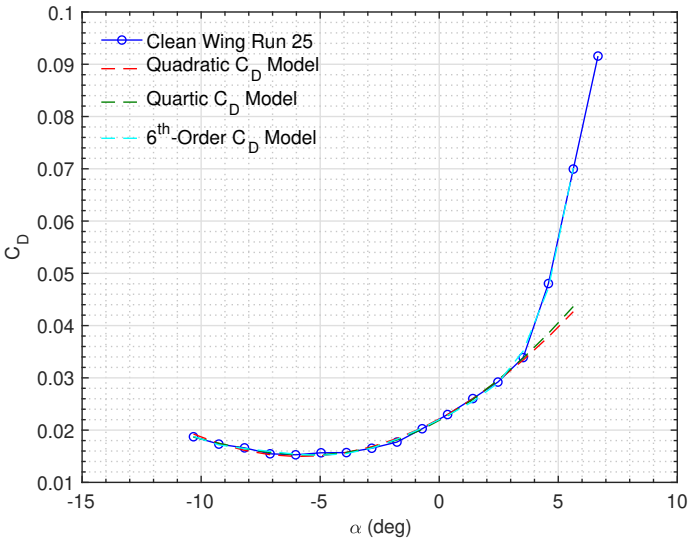

Figure 53. Drag Coefficient Correlation for Run 25 (June 2018)

A series of test runs were conducted on June 29 using the iterative angle-of-attack seeking method for the first time to speed up the test. The following specific procedures were implemented:

- Conduct a clean wing angle-of-attack sweep from $\alpha = -6^\circ$ to $\alpha = 6^\circ$.
- Set the wing at the trial optimal angle of attack $\alpha^* = \bar{\alpha} - 0.5^\circ$ where $\bar{\alpha}$ is the clean wing angle of attack at the off-design $C_L^* = 0.65$ or $C_L^* = 0.7$

- Set the flap position for each of the flap segments to 2°, 4°, and 6° for each run while keeping all the other flap positions at zero.
- Compute the optimal solution using the iterative optimization method which can better handle the nonlinear lift coefficient and drag coefficient models. This results in the new optimal angle of attack α^* and flap position vectors δ^*.
- Set the wing at the new flap position vector δ^* and conduct an angle of attack sweep.
- Set the wing at the new optimal angle of attack α^* and perturb the flap position for each of the flap segments $\pm 2°$ about their respective optimal flap positions to perform the iterative refinement optimization. This results in the improved optimal angle of attack α^* and flap position vectors δ^*.
- Set the wing at the new flap position vector δ^* and conduct an angle of attack sweep.
- If the drag coefficient at the off-design C_L^* is less than the clean wing drag coefficient, the optimization is completed.

It should be noted that the flap settings in these series of test runs were performed manually with the flap positions verified with an inclinometer. This is due to the gradual degradation of the flap servos, thereby preventing them from being commanded properly by the control system.

The BLS algorithm is used to perform the parameter estimation during the iterative angle-of-attack seeking procedure. Figures 54 and 55 show the incremental lift and drag coefficient estimates computed by the BLS algorithm. It can be seen that Flap 1B is the most dominant flap that produces the largest incremental lift and drag coefficients. Flaps 2B, 4B, and 6B have negative slopes in the incremental drag coefficient which are unexpected. There is a high degree of data scatter in the BLS parameter estimation due to the uncertainty in the flap positions.

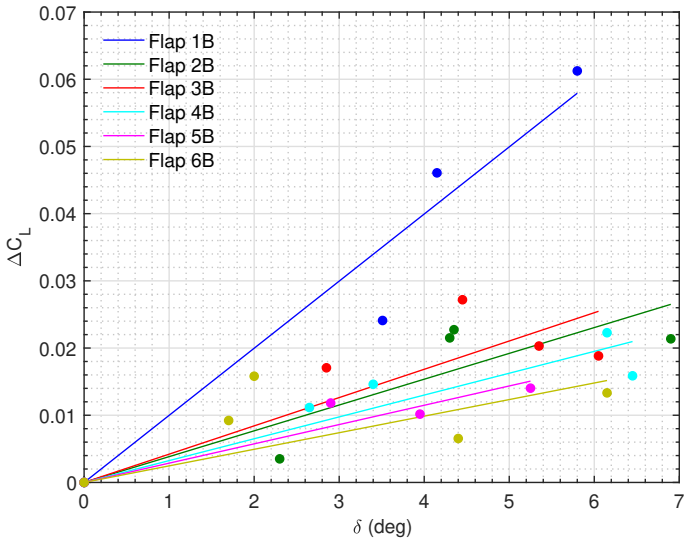

Figure 54. Incremental Lift Estimated by BLS (June 2018)

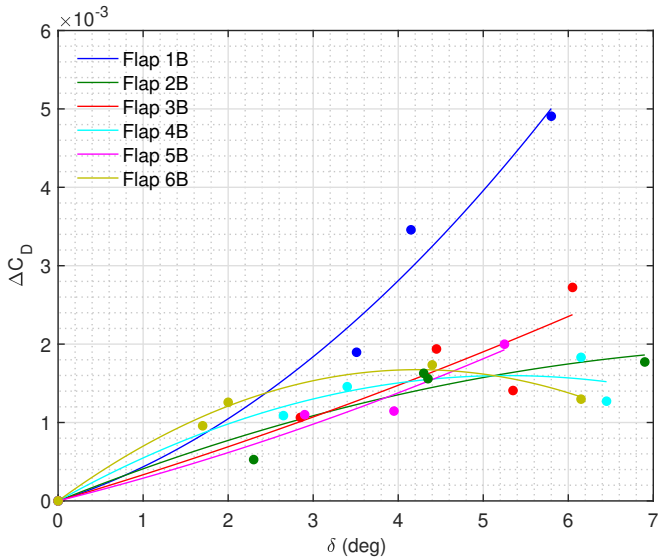

Figure 55. Incremental Drag Coefficient Estimated by BLS (June 2018)

In addition to the off-design $C_L^* = 0.65$, the off-design $C_L^* = 0.7$ is also chosen because the L/D of the clean wing shows that the maximum L/D ratio occurs very close to $C_L = 0.65$ as can be seen in Fig. 51. By selecting the off-design C_L^* where the L/D ratio is not too close to its maximum value, the drag optimization may have a reasonable chance of finding feasible solutions.

Using the parameter estimates, the iterative gradient optimization method is implemented to compute 11 candidate optimal solutions. In addition, four pseudo-inverse optimization solutions are computed. In the optimization, four different flap options are considered: 1) optimization with all the flap segments, 2) optimization with only Flap 1B since it is the most dominant flap segment, 3) optimization with Flap 5B removed since it consistently shows a negative value in the iterative gradient optimization, and 4) optimization with both Flaps 3B and 5B removed for the same reason as the reason for removing Flap 5B. These solutions are presented in Table 2. It can be seen from Table 2 that the computed drag coefficients C_D^* corresponding to $C_L^* = 0.65$ for the optimization are in all but one cases indeed are greater than the clean wing drag coefficient $\bar{C}_D$. This confirms the possibility of infeasible solutions for the off-design C_L^* near the maximum L/D ratio.

Because of the lack of time, only a select few of these solutions; namely, OS 1, OS 3, OS 9, PS 1, and PS 3, were actually conducted on July 2 when the test was in the final day. Also because of the lack of time, the iterative refinement optimization was not implemented. Table 3 shows the results of the five optimization runs. The OS 1 computed by the iterative gradient optimization method yields the largest drag reduction among the three OS 1, OS 3, and OS 9. It achieves a 5 count or 2.0% drag reduction for the design $C_L = 0.5$, 13 count or 3.9% drag reduction for the off-design $C_L^* = 0.65$, and 18 count or 4.7% drag reduction for the off-design $C_L^* = 0.7$. The pseudo-inverse optimization method interestingly enough produces the largest drag reduction for the off-design $C_L^* = 0.7$ of 36 counts or 9.4% with the PS 3. The pseudo-inverse optimization method produces varying degrees of drag reduction in all cases for the off-design $C_L^* = 0.65$ and $C_L^* = 0.7$.

Solution	C_L^*	$\bar{C}_D$	C_D^*	α^*	δ_{1B}^*	δ_{2B}^*	δ_{3B}^*	δ_{4B}^*	δ_{5B}^*	δ_{6B}^*
OS 1 (All Flaps)	0.7	373	346	3.14	2.15	3.22	−0.62	3.21	−1.70	3.26
OS 2 (Flaps 3B & 5B Removed)	0.7	373	349	3.01	2.82	2.26	0	2.87	0	3.11
OS 3 Run 54 (Flap 1B Only)	0.7	373	327	3.27	3.66	0	0	0	0	0
OS 4 (All Flaps [(1)])	0.7	373	353	2.90	2.52	3.20	1.89	3.00	−1.18	3.35
OS 5 (Flap 5B Removed [(1)])	0.7	373	355	2.85°	2.37	3.45	2.00	3.13	0	3.38
OS 6 (Flap 1B Only [(1)])	0.7	373	327	3.27	3.66	0	0	0	0	0
OS 7 (All Flaps)	0.65	320	336	2.67	1.22	4.57	−3.61	3.68	−3.01	3.48
OS 8 (3B & 5B Removed)	0.65	320	340	2.33	1.00	4.90	0	3.80	0	3.54
OS 9 (Flap 1B Only)	0.65	320	315	2.86	1.37	0	0	0	0	0
OS 10 (All Flaps [(1)])	0.65	320	344	2.19	0.92	5.88	3.09	4.39	−3.44	3.69
OS 11 (Flap 5B Removed [(1)])	0.65	320	346	2.04	0.84	6.01	3.15	4.46	0	3.71
PS 1 (All Flaps)	0.7	373	337	3.14	2.85	1.10	1.20	0.93	0.82	0.70
PS 2 (All Flaps [(1)])	0.7	373	347	2.90	3.71	1.29	1.83	1.43	1.07	0.78
PS 3 (All Flaps)	0.65	320	322	2.67	1.68	0.65	0.71	0.55	0.48	0.42
PS4 (All Flaps [(1)])	0.65	320	338	2.19	3.64	1.26	1.79	1.40	1.05	0.77

Table 2. Iterative Optimization and Pseudo-Inverse Optimization Solutions

Notes:
[(1)]: Without repeat data points included - these data points are taken when there are questions about test results.
$\bar{C}_D$: Computed clean wing drag coefficient at the corresponding C_L^* in counts
C_D^*: Computed drag coefficient at the corresponding C_L^* for corresponding solution in counts
OS: Optimal Solution computed by iterative gradient optimization
PS: Pseudo-Inverse Solution computed by pseudo-inverse optimization
All angles of attack and flap positions are in degrees.

	Design $C_L = 0.5$		Off-Design $C_L^* = 0.65$		Off-Design $C_L^* = 0.7$	
Run	C_D	ΔC_D	C_D	ΔC_D	C_D	ΔC_D
Clean Wing Run 56	253	0	330	0	382	0
OS 1 Run 53	248	5	317	13	364	18
OS 3 Run 54	255	-2	321	9	367	15
OS 9 Run 55	256	-3	329	1	376	6
PS 1 Run 57	259	-6	322	8	360	22
PS 3 Run 58	252	1	321	9	346	36

Table 3. Drag Optimization Wind Tunnel Test Results

Figure 56 shows the lift curves for the optimization runs. Figure 57 shows the plot of the drag polars for the optimization runs. It can be seen that the OS 1 optimization Run 53 shows a considerable drag reduction over the clean wing for a wide range of the lift coefficient from $C_L = 0$ to $C_L = 0.79$.

Figure 58 shows the plot of the L/D curves for the optimization runs. It can be seen that the OS 1 optimization Run 53 produces the largest maximum L/D ratio of 20.95 as compared to the clean wing L/D ratio of 20.15, a 4% increase. The PS 3 optimization Run 58 achieves the maximum L/D ratio of 20.21 over the widest range of the lift coefficient from $C_L = 0.53$ to $C_L = 0.72$, thus resulting in a larger drag reduction than all other optimization runs.

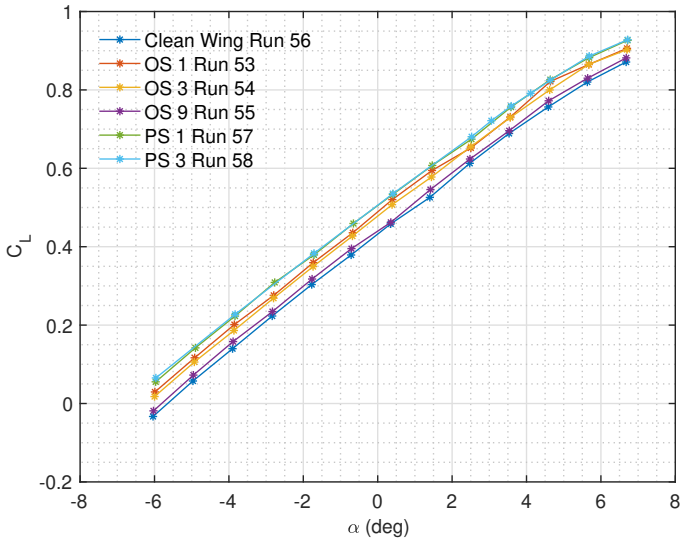

Figure 56. Lift Curves of Optimization Runs (July 2, 2018)

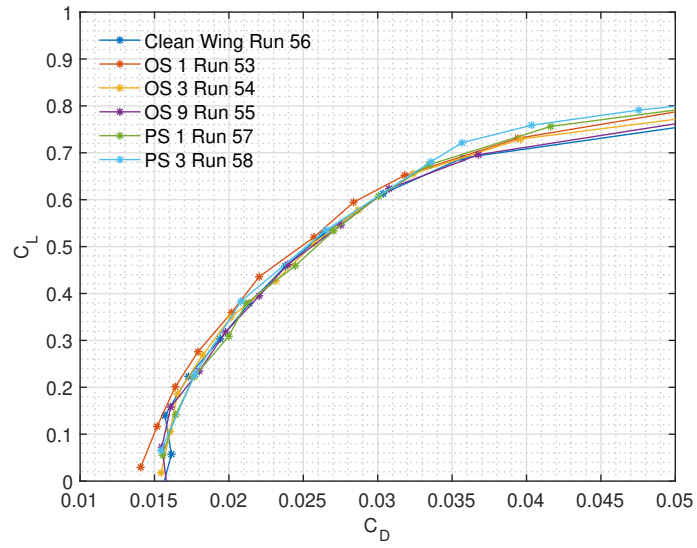

Figure 57. Drag Polars of Optimization Runs (July 2, 2018)

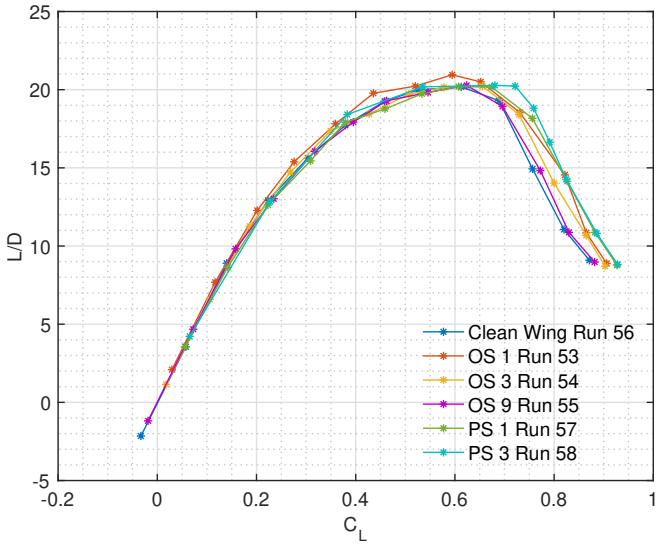

Figure 58. L/D **Curves of Optimization Runs (July 2, 2018)**

VI. Conclusions

A real-time drag optimization experimental investigation has been presented. The real-time drag optimization wind tunnel test was conducted in the University of Washington Aeronautical Laboratory (UWAL). The wind tunnel model is a CRM (Common Research Model) wing with a modified wing flexibility to achieve a wing tip deflection of 10% of the wing semi-span. The open CRM geometry is modified to incorporate an optimized jig shape twist computed by an aero-structural optimization using CART3D to account for the modified wing flexibility. The wing is a complex design with an actively controlled variable camber continuous trailing edge flap (VCCTEF) system comprising twelve individual control surfaces. Each of the control surfaces is driven by a servo mechanism commanded by a control system. The real-time drag optimization strategy includes an onboard aerodynamic model identification which performs model parameter estimation using a recursive least-squares (RLS) algorithm and a batch least-squares (BLS) algorithm. Several real-time drag optimization methods are developed.

The wind tunnel test was conducted in three test entries over a period from September 2017 to July 2018. The first test entry in September 2017 identified major hardware issues with the flap servo mechanisms and related problems. These issues were traced to the overheating and overloading problems with the servos. These issues caused the test to be aborted prematurely. A redesign effort ensued to upgrade the servos with a more robust design.

The second test entry took place in April 2018. The test was able to proceed without major hardware issues. However, an issue was identified with the onboard aerodynamic model identification RLS algorithm. The parameter estimates computed by the RLS algorithm failed to converge to their correct values due to an initialization problem in the algorithm, resulting in inaccuracy in the lift and drag predictions by the onboard aerodynamic model. As a result, the real-time drag optimization failed to work properly.

During the second test entry, the silicone rubber transition inserts for the VCCTEF were removed due to cracking and because they also cause overloading of the servos. Plastic inserts were fabricated and installed in the flap gaps to bring the flap side edges closer to within 1/16 of an inch. The resulting flap configuration is referred to as a variable camber discrete trailing edge flap (VCDTEF) system. The VCCTEF later was restored with new 3D-printed transition inserts. These two types of flap designs were tested and the data show a considerable reduction in the angle of attack and drag reduction at the same lift coefficient. The VCCTEF produces less drag by 13 counts or 5% at the design lift coefficient than the VCDTEF which confirms the benefit of the VCCTEF.

The third and final test entry took place in June 2018. Several changes and improvements were made to the software and the real-time drag optimization strategy. An iterative angle-of-attack seeking method is developed and implemented in the test to speed up the real-time optimization process. Three additional optimization methods are developed: the iterative gradient optimization, the pseudo-inverse optimization, and the analytical optimization. The

onboard aerodynamic model identification RLS algorithm was able to perform parameter estimation properly. The real-time drag optimization using the analytical optimization method produces 8 count or 2.4% drag reduction at the off-design lift coefficient of 0.65. The iterative angle-of-attack seeking method was conducted in the latter part of the test when the servos began to experience issues. The onboard aerodynamic model identification was performed using the BLS algorithm. The iterative gradient optimization and the pseudo-inverse optimization are used to compute several candidate optimal solutions. Some of these solutions were verified experimentally in the test. The iterative gradient optimization produces up to 18 count or 4.7% drag reduction for the off-design lift coefficient of 0.7. The pseudo-inverse optimization which does not require the drag coefficient model is found to be quite effective in reducing drag. Up to 36 count or 9.4% drag reduction for the off-design lift coefficient of 0.7 is achieved with the pseudo-inverse optimization.

In summary, the objectives of the real-time drag optimization experimental investigation have been successfully demonstrated. The methods developed in this investigation could provide new capabilities to enable future adaptive wing technologies for next-generation aircraft to further improve fuel economy.

Acknowledgment

The authors wish to acknowledge NASA Advanced Air Transport Technologies project for the funding support of this work. The authors also acknowledge the funding for the wind tunnel experiment under NASA SBIR Phase II Contract NNX15CA16C

References

[1]Nguyen, N., "Elastically Shaped Future Air Vehicle Concept," NASA Innovation Fund Award 2010 Report, October 2010, Submitted to NASA Innovative Partnerships Program, http://ntrs.nasa.gov/archive/nasa /casi.ntrs.nasa.gov/20110023698.pdf

[2]Nguyen, N. and Urnes, J., "Aeroelastic Modeling of Elastically Shaped Aircraft Concept via Wing Shaping Control for Drag Reduction," AIAA Atmospheric Flight Mechanics Conference, AIAA-2012-4642, August 2012.

[3]Nguyen, N., Trinh, K., Reynolds, K., Kless, J., Aftosmis, M., Urnes, J., and Ippolito, C., "Elastically Shaped Wing Optimization and Aircraft Concept for Improved Cruise Efficiency," 51st AIAA Aerospace Sciences Meeting, AIAA-2013-0141, January 2013.

[4]Boeing Report No. 2012X0015, "Development of Variable Camber Continuous Trailing Edge Flap System," Submitted to NASA, October 4, 2012.

[5]Urnes, J., Nguyen, N., Ippolito, C., Totah, J., Trinh, K., and Ting, E., "A Mission Adaptive Variable Camber Flap Control System to Optimize High Lift and Cruise Lift to Drag Ratios of Future N+3 Transport Aircraft," 51st AIAA Aerospace Sciences Meeting, AIAA-2013-0214, January 2013.

[6]Boeing Report No. 2014X0030, "Development of Variable Camber Continuous Trailing Edge Flap System for B757 Configured with a More Flexible Wing," Submitted to NASA, September 27, 2014.

[7]Urnes, J., Morris, C., Sheahan, J., Dykman, J., and Klingman, D., "Control System Design for a Variable Camber Continuous Trailing Edge Flap System on an Elastic Wing," 55th AIAA/ASME/ASCE/AHS/ASC Structures, Structural Dynamics, and Materials Conference, AIAA-2014-0835, January 2014.

[8]Dykman, J., Truong, H., and Urnes, J., "Active Control for Elastic Wing Structure Dynamic Modes," 56th AIAA/ASCE/AHS/ASC Structures, Structural Dynamics, and Materials Conference, AIAA-2015-1842, January 2015.

[9]Ferrier, Y., Nguyen, N., and Ting, E., "Real-Time Adaptive Least-Squares Drag Minimization for Performance Adaptive Aeroelastic Wing," 34th AIAA Applied Aerodynamics Conference, AIAA-2016-3567, June 2016.

[10]Nguyen, N., Precup, N., Urnes, J., Nelson, C., Lebofsky, S., Ting, E., and Livne, E., "Experimental Investigation of a Flexible Wing with a Variable Camber Continuous Trailing Edge Flap Design," 32nd AIAA Applied Aerodynamics, AIAA 2014-2441, June 2014.

[11]Precup, N., Mor, M., and Livne, E., "Design, Construction, and Tests of an Aeroelastic Wind Tunnel Model of a Variable Camber Continuous Trailing Edge Flap (VCCTEF) Concept Wing," 32nd AIAA Applied Aerodynamics Conference, AIAA-2014-2442, June 2014.

[12]Nguyen, N., Precup, N., Livne, E., Urnes, J., Dickey, E., Nelson, C., Chiew, J., Rodriguez, D., Ting, E., and Lebofsky, S., "Wind Tunnel Investigation of a Flexible Wing High-Lift Configuration with a Variable Camber Continuous Trailing Edge Flap Design," 33rd AIAA Applied Aerodynamics Conference, AIAA-2015-2417, June 2015.

[13]Precup, N., Mor, M., and Livne, E., "The Design, Construction, and Tests of a Concept Aeroelastic Wind Tunnel Model of a High-Lift Variable Camber Continuous Trailing Edge Flap (HL-VCCTEF) Wing Configuration," 56th AIAA/ASCE/AHS/ASC Structures, Structural Dynamics, and Materials Conference, AIAA-2015-1406, January 2015.

[14]Vassberg, J., Dehaan M., Rivers, M., and Wahls, R., "Development of a Common Research Model for Applied CFD Validation Studies," 26th AIAA Applied Aerodynamics Conference, AIAA-2008-6919, August 2008.

[15]Precup, N., Mundt, T., Mor, M., Livne, E., "An Active Variable Camber Continuous Trailing Edge Flapped Wing Wind Tunnel Model for Aeroelastic "In-Flight" Shape Optimization Tests," AIAA Multidisciplinary Analysis and Optimization Conference, AIAA-2018-3106, June 2018.

[16]Ting, E., Chaparro, D., Nguyen, N., and Fujiwara, G., "Optimization of Variable Camber Continuous Trailing Edge Flap Configuration for Drag Reduction," AIAA Journal of Aircraft, Vol. 55, No. 6, pp. 2217-2239, November 2018.